



**NAVAL
POSTGRADUATE
SCHOOL**

MONTEREY, CALIFORNIA

THESIS

**MODELLING THE PERFORMANCE OF AND ANALYZING
THERMAL RADIANCE REDUCTION BY A WATER-COOLED
THERMOELECTRIC WASTE HEAT HARVESTING SYSTEM
AND THE DEVELOPMENT OF AN AIR-COOLED HEAT SINK
REPLACEMENT**

by

Daniel L. Sloan

June 2020

Thesis Advisor:
Co-Advisor:

Dragoslav Grbovic
Anthony G. Pollman

Approved for public release. Distribution is unlimited.

THIS PAGE INTENTIONALLY LEFT BLANK

REPORT DOCUMENTATION PAGE			<i>Form Approved OMB No. 0704-0188</i>
Public reporting burden for this collection of information is estimated to average 1 hour per response, including the time for reviewing instruction, searching existing data sources, gathering and maintaining the data needed, and completing and reviewing the collection of information. Send comments regarding this burden estimate or any other aspect of this collection of information, including suggestions for reducing this burden, to Washington headquarters Services, Directorate for Information Operations and Reports, 1215 Jefferson Davis Highway, Suite 1204, Arlington, VA 22202-4302, and to the Office of Management and Budget, Paperwork Reduction Project (0704-0188) Washington, DC 20503.			
1. AGENCY USE ONLY (Leave blank)	2. REPORT DATE June 2020	3. REPORT TYPE AND DATES COVERED Master's thesis	
4. TITLE AND SUBTITLE MODELLING THE PERFORMANCE OF AND ANALYZING THERMAL RADIANCE REDUCTION BY A WATER-COOLED THERMOELECTRIC WASTE HEAT HARVESTING SYSTEM AND THE DEVELOPMENT OF AN AIR-COOLED HEAT SINK REPLACEMENT			5. FUNDING NUMBERS
6. AUTHOR(S) Daniel L. Sloan			
7. PERFORMING ORGANIZATION NAME(S) AND ADDRESS(ES) Naval Postgraduate School Monterey, CA 93943-5000			8. PERFORMING ORGANIZATION REPORT NUMBER
9. SPONSORING / MONITORING AGENCY NAME(S) AND ADDRESS(ES) N/A			10. SPONSORING / MONITORING AGENCY REPORT NUMBER
11. SUPPLEMENTARY NOTES The views expressed in this thesis are those of the author and do not reflect the official policy or position of the Department of Defense or the U.S. Government.			
12a. DISTRIBUTION / AVAILABILITY STATEMENT Approved for public release. Distribution is unlimited.			12b. DISTRIBUTION CODE A
13. ABSTRACT (maximum 200 words) <p>Propulsion and electrical generator systems that utilize fossil fuels experience losses in efficiencies due to waste heat. While there are a number of ways to recover some of this waste heat, this research focuses on a waste heat harvesting system that uses thermoelectric generators (TEGs). TEGs operate via the Seebeck effect, where a temperature difference generates an electric potential. This project consists of three parts. The first part details the steps taken to model the existing water-cooled thermoelectric waste heat harvesting prototype using COMSOL Multiphysics Finite Element Analysis Software. The second part analyzes how well the water-cooled prototype reduces the thermal signature of the gasoline-powered generator's muffler. This application shows that it could be useful in minimizing asset visibility in the infrared spectrum for expeditionary missions. The last part discusses the design, fabrication, and performance of a passive, air-cooled variant of the thermoelectric waste heat harvesting system. When water-cooled applications are not feasible, as with expeditionary vehicles, having an air-cooled version is possible.</p>			
14. SUBJECT TERMS thermoelectric generator, TEG, waste heat recovery, waste heat harvesting, IR signature reduction, thermal signature reduction			15. NUMBER OF PAGES 99
			16. PRICE CODE
17. SECURITY CLASSIFICATION OF REPORT Unclassified	18. SECURITY CLASSIFICATION OF THIS PAGE Unclassified	19. SECURITY CLASSIFICATION OF ABSTRACT Unclassified	20. LIMITATION OF ABSTRACT UU

THIS PAGE INTENTIONALLY LEFT BLANK

Approved for public release. Distribution is unlimited.

**MODELLING THE PERFORMANCE OF AND ANALYZING THERMAL
RADIANCE REDUCTION BY A WATER-COOLED THERMOELECTRIC
WASTE HEAT HARVESTING SYSTEM AND THE DEVELOPMENT OF AN
AIR-COOLED HEAT SINK REPLACEMENT**

Daniel L. Sloan
Lieutenant, United States Navy
BSAE, University of Tennessee, 2009

Submitted in partial fulfillment of the
requirements for the degree of

MASTER OF SCIENCE IN APPLIED PHYSICS

from the

**NAVAL POSTGRADUATE SCHOOL
June 2020**

Approved by: Dragoslav Grbovic
Advisor

Anthony G. Pollman
Co-Advisor

Kevin B. Smith
Chair, Department of Physics

THIS PAGE INTENTIONALLY LEFT BLANK

ABSTRACT

Propulsion and electrical generator systems that utilize fossil fuels experience losses in efficiencies due to waste heat. While there are a number of ways to recover some of this waste heat, this research focuses on a waste heat harvesting system that uses thermoelectric generators (TEGs). TEGs operate via the Seebeck effect, where a temperature difference generates an electric potential. This project consists of three parts. The first part details the steps taken to model the existing water-cooled thermoelectric waste heat harvesting prototype using COMSOL Multiphysics Finite Element Analysis Software. The second part analyzes how well the water-cooled prototype reduces the thermal signature of the gasoline-powered generator's muffler. This application shows that it could be useful in minimizing asset visibility in the infrared spectrum for expeditionary missions. The last part discusses the design, fabrication, and performance of a passive, air-cooled variant of the thermoelectric waste heat harvesting system. When water-cooled applications are not feasible, as with expeditionary vehicles, having an air-cooled version is possible.

THIS PAGE INTENTIONALLY LEFT BLANK

TABLE OF CONTENTS

I.	INTRODUCTION.....	1
A.	BACKGROUND	1
B.	THERMOELECTRIC GENERATORS	2
C.	PREVIOUS RESEARCH PERFORMED USING TEGS.....	4
1.	Automotive Research.....	4
2.	Military Application Research.....	6
D.	REDUCING THE INFRARED SIGNATURE	6
II.	COMSOL MODEL OF WATER-COOLED THERMOELECTRIC WASTE HEAT HARVESTING PROTOTYPE	7
A.	BUILDING THE MODEL USING THERMAL DATA	7
B.	RESULTS AND ANALYSIS	20
1.	Model Using the Thermal Data	20
2.	Adjusting the Model to Match Experimental Data	29
III.	ASSESSING THERMAL RADIANCE REDUCTION OF THE THERMOELECTRIC WASTE HEAT HARVESTING PROTOTYPE	35
A.	DATA COLLECTION METHOD	35
1.	Thermal Imaging and Emissivity Estimates.....	35
2.	Radiant Power Estimations.....	38
3.	Predicting Maximum Detection Ranges	41
B.	RESULTS	44
IV.	DEVELOPMENT AND FABRICATION OF AIR-COOLED RADIATOR ATTACHMENT FOR THERMOELECTRIC WASTE HEAT HARVESTING PROTOTYPE	47
A.	DESIGNING AND FABRICATING THE PASSIVE COOLER.....	47
B.	ASSESSING THE THERMAL RADIANCE REDUCTION OF THE AIR-COOLED HEAT SINK	50
C.	COMSOL MODEL OF AIR-COOLED THERMOELECTRIC WASTE-HEAT HARVESTING PROTOTYPE.....	53
V.	CONCLUSION	63
A.	ANALYSIS OF RESULTS.....	63
B.	PROPOSED FUTURE WORK	64
	APPENDIX A. MATLAB CODE FOR CALCULATING CONVECTIVE HEAT TRANSFER COEFFICIENTS.....	65

A.	H VALUE FOR MUFFLER	65
B.	H VALUE FOR WATER COOLER	66
C.	H VALUE FOR PASSIVE RADIATOR	66
APPENDIX B.	MATLAB CODE FOR NEP CALCULATIONS AND RADIANT POWER PLOT	69
A.	INITIAL TEST	69
B.	INCLUDING RADIATOR	71
APPENDIX C.	COMSOL INPUT PARAMETERS.....	73
A.	MATERIALS	73
B.	ADJUSTED WATER-COOLED MODEL	73
C.	AIR-COOLED MODEL	74
LIST OF REFERENCES		75
INITIAL DISTRIBUTION LIST		79

LIST OF FIGURES

Figure 1.	Illustration of the Seebeck Effect in a thermoelectric generator (TEG). Source: [6].	3
Figure 2.	Internal schematic of a thermoelectric generator (TEG) module. Source: [4].	3
Figure 3.	TEG module model TE-MOD-22W7V-56. Source: [8].	4
Figure 4.	Water-cooled thermoelectric generator waste heat harvesting prototype. Source: [15].	8
Figure 5.	Isolated view of the muffler. Source: [16].	8
Figure 6.	A semi-transparent model of the muffler built in COMSOL.	9
Figure 7.	FLIR image of the muffler in ResearchIR, with data given on the mean surface temperature within the region of interest (ROI), shown as a red box.	9
Figure 8.	Temperature profile of the muffler model in COMSOL.	13
Figure 9.	FLIR image of the muffler.	13
Figure 10.	Model of the muffler and base plate built in COMSOL.	14
Figure 11.	Semi-transparent COMSOL model of the detailed TEG module. Source: [20].	15
Figure 12.	Semi-transparent COMSOL model of the simplified TEG module. Source: [20].	15
Figure 13.	COMSOL model of simplified TEG modules on the base plate, which is attached to the muffler.	17
Figure 14.	Water channels inside of the water cooler.	17
Figure 15.	Semi-transparent COMSOL model of the water cooler.	18
Figure 16.	Final COMSOL model of the water-cooled prototype.	18
Figure 17.	Water-cooled prototype.	19
Figure 18.	Temperature profile from simulation performed on the final model in COMSOL.	21

Figure 19.	FLIR image of water-cooled prototype.....	21
Figure 20.	Graphical representation of the hot side and cool side data for both the experimental and COMSOL simulation temperature readings.....	23
Figure 21.	Differential temperatures plotted for each TEG module for both the experimental and COMSOL values	24
Figure 22.	Differential temperature for the experimental data and the simulation values arranged from lowest highest.....	26
Figure 23.	Current vs. load resistance for the average experimental values, theoretical values using the experimental differential temperatures, and the COMSOL model's theoretical values	27
Figure 24.	Voltage vs. load resistance for the average experimental values, theoretical values using the experimental differential temperatures, and the COMSOL model's theoretical values	28
Figure 25.	Power vs. load resistance for the average experimental values, theoretical values using the experimental differential temperatures, and the COMSOL model's theoretical values	28
Figure 26.	Graphical representation of the hot side and cool side data for both the experimental and the adjusted COMSOL simulation temperature readings.....	31
Figure 27.	Differential temperature for the experimental data and the adjusted simulation values arranged from lowest highest.....	31
Figure 28.	Current vs. load resistance for the average experimental values, theoretical values using the experimental differential temperatures, and the adjusted COMSOL model's theoretical values	32
Figure 29.	Voltage vs. load resistance for the average experimental values, theoretical values using the experimental differential temperatures, and the adjusted COMSOL model's theoretical values	33
Figure 30.	Power vs. load resistance for the average experimental values, theoretical values using the experimental differential temperatures, and the adjusted COMSOL model's theoretical values	33
Figure 31.	FLIR image of the muffler in ResearchIR software showing the rectangular region of interest (ROI) and window giving the radiance statistics for this ROI.	37

Figure 32.	Radiant power plotted over a range of distances from the source (muffler with no attachments) with trend line shown as a black dotted line, and trend line equation and associated root mean squared value given	39
Figure 33.	Radiant power plotted over a range of distances from the source (muffler with TEG assembly attached, but no water flowing through cooler) with trend line shown as a black dotted line, and trend line equation and associated root mean squared value given	40
Figure 34.	Radiant power plotted over a range of distances from the source (muffler with TEG assembly attached and water flowing through cooler) with trend line shown as a black dotted line, and trend line equation and associated root mean squared value given	40
Figure 35.	Scorpio LW IDCA. Source: [28].	42
Figure 36.	Daphnis-HD MW IDCA. Source: [29].	42
Figure 37.	Radiant power vs. distance from source for each configuration of the generator’s muffler, along with the NEPs for three different IR detectors	43
Figure 38.	Final design of the passive cooler in SolidWorks.....	48
Figure 39.	Fabricated radiator	48
Figure 40.	Radiator affixed to base plate, enclosing the TEG modules.....	49
Figure 41.	Air-cooled thermoelectric waste heat harvesting prototype	49
Figure 42.	Radiant power plotted over a range of distances from the source (muffler with air-cooled radiator) with trend line shown as a black dotted line, and trend line equation and associated root mean squared value given	51
Figure 43.	Radiant power vs. distance from the source for each configuration of the generator’s muffler, along with the NEPs for three different IR detectors	52
Figure 44.	COMSOL model of radiator	54
Figure 45.	Exposed TEG modules due to shortened radiator length and misalignment of bolts.....	54
Figure 46.	COMSOL model of air-cooled prototype	55

Figure 47.	FLIR image of the radiator in ResearchIR, with data given on the mean surface temperature within the region of interest (ROI), shown as a red box	56
Figure 48.	Temperature profile from heat transfer simulation for the air-cooled prototype model in COMSOL	57
Figure 49.	FLIR image of the generator with the air-cooled prototype attached	57
Figure 50.	Differential temperatures from COMSOL simulations using both water-cooled and air-cooled heat sink designs	59
Figure 51.	Theoretical current vs. load resistances for COMSOL models using water-cooled and air-cooled heat sinks	60
Figure 52.	Theoretical voltage vs. load resistances for COMSOL models using water-cooled and air-cooled heat sinks	61
Figure 53.	Theoretical power vs. load resistances for COMSOL models using water-cooled and air-cooled heat sinks	61

LIST OF TABLES

Table 1.	Average differential temperatures from the COMSOL model when using different ceramic materials inside of the TEG modules.....	20
Table 2.	Average experimental temperature measurements on TEG modules operating in prototype assembly. Source: [15].	22
Table 3.	Temperature measurements on TEG modules derived from COSMOL model.....	23
Table 4.	Average experimental voltage and current readings across a load resistor, generated by the water-cooled prototype, with resulting power. Source: [15].....	25
Table 5.	Theoretical voltage, current, and power values across a load resistor, derived from TEG module open circuit voltage and internal resistance equations, as a function of differential temperatures obtained from COSMOL model	27
Table 6.	Temperature measurements on TEG modules derived from the adjusted COSMOL model.....	30
Table 7.	Theoretical voltage, current, and power values across a load resistor, derived from TEG module open circuit voltage and internal resistance equations, as a function of differential temperatures obtained from the adjusted COSMOL model	32
Table 8.	Temperature measurements and emissivity estimates	37
Table 9.	Mean radiance data recorded for the muffler in three different configurations	38
Table 10.	Theoretical maximum detection ranges for selected IR detectors and the generator’s muffler in various configurations.....	44
Table 11.	Mean radiance of the radiator	50
Table 12.	Theoretical maximum detection ranges for selected IR detectors and the generator’s muffler in various configurations.....	53
Table 13.	Temperature measurements on TEG modules derived from COSMOL model.....	58
Table 14.	Theoretical voltage, current, and power values across load resistances, derived from TEG module open-circuit voltage and	

internal resistance equations, as a function of differential
temperatures obtained from COSMOL model using an air-cooled
heat sink60

LIST OF ACRONYMS AND ABBREVIATIONS

AETEG	Automotive exhaust thermoelectric generator
CEC	California Energy Commission
COTS	Commercial-off-the-shelf
DOD	Department of Defense
DOE	Department of Energy
DON	Department of the Navy
EMF	Electromotive force
FLIR	Forward Looking Infrared
FPA	Focal plane area
IDCA	integrated Dewar cooler assembly
IR	Infrared
LWIR	Long wavelength infrared
MWIR	Medium wavelength infrared
NEP	Noise equivalent power
NETD	Noise equivalent temperature difference
NPS	Naval Postgraduate School
ROI	Region of interest
TEG	Thermoelectric generator

THIS PAGE INTENTIONALLY LEFT BLANK

ACKNOWLEDGMENTS

I would like to take this opportunity to thank Dr. Grbovic for his assistance in helping me understand how to use COMSOL, as well as for his and Dr. Pollman's guidance and support throughout this project. I would like to thank Dr. Alves for taking the time to teach me how to use the FLIR camera and the ResearchIR software. Additionally, I would like to voice my appreciation to Ben McHale for giving me pointers on how to use SolidWorks. I also express my gratitude to Lauren Howard and all the others who have worked on this project before me—we would not be at this point in the research without your efforts. Last, but certainly not least, I want to thank my wife, Joyce Sloan, for her love and support throughout my academic and Navy careers.

THIS PAGE INTENTIONALLY LEFT BLANK

I. INTRODUCTION

A. BACKGROUND

Increasing the overall energy efficiency of military ships, vehicles, and equipment can go a long way in bolstering the capabilities of that fighting force. Even minor improvements in energy efficiency can help reduce costs, reduce the frequency of resupply, and increase the range and endurance of these military platforms. In 2009, the Secretary of the Navy at the time, the honorable Ray Mabus, called for changes in how the Department of the Navy (DON) generates and uses energy [1]. Secretary Mabus' directive [2] dealt primarily with finding fuel and energy alternatives, but it also called for finding ways to improve the efficiency of what the DON currently employs. The DON is the second largest consumer of petroleum fuel within the Department of Defense (DOD) [1]. As of 2008, 57% of the DON consumed petroleum fuel with the breakdown of that usage as follows: 40% for aviation units, 38% for maritime units, 16% for expeditionary units, and 6% for shore facilities [2].

Common prime movers utilized by the DON that consume petroleum fuel are internal combustion engines and gas turbine engines. Typical thermal efficiencies for these engines [3] are as follows: 30% to 40% for high-speed diesels engines, typically found in trucks; around 45% for large, slow-speed, marine diesel engines; and anywhere from 20% up to 40% for gas turbine engines. Focusing only on the engine, anywhere from 55% to 80% of the total input energy is wasted. Not only does this wasted heat energy count as a loss to the system, it also generates a large thermal signature in the infrared (IR) spectrum, making the platform vulnerable to a variety of surveillance and targeting systems.

Considerable research has been done in the field of waste heat energy recovery, or waste heat energy harvesting. The goal is to find methods by which the overall energy efficiency can be increased. One focus of this type of research is to use thermoelectric generators (TEGs). This thesis paper continues the efforts performed to date by the Naval Postgraduate School (NPS) on using TEGs for waste heat energy harvesting in the following ways: modeling the existing, water-cooled prototype via COMSOL Multiphysics

software; assessing how the IR signature of an exhaust system is reduced by using the prototype; and exploring how the prototype can be passively cooled by the ambient air instead of water, which could help reduce the weight that would otherwise be added by pumps, water reservoirs, etc.

B. THERMOELECTRIC GENERATORS

Thermoelectric generators (TEGs) operate using the Seebeck Effect [4]. The Seebeck Effect is named for Thomas Johann Seebeck, who discovered it. When one end of a conductor is heated, whether a metal or a semiconductor, a temperature difference, ΔT , is generated, along with a temperature gradient, $\vec{\nabla}T$, from the cold end to the heated end. Among other effects, this temperature gradient causes a change in the Fermi energy, E_F , at the heated end and generates an electromotive force (EMF). A potential difference is induced by the generated and separated carriers, which is proportional to the temperature difference. This potential is known as the Seebeck voltage.

To harness the Seebeck Effect [4], p- and n-type semiconductors with different Seebeck coefficients are connected by way of a conducting metal. The Seebeck coefficient [5], widely known as the thermoelectric power, is a temperature-dependent material property. When subjected to a temperature gradient, electron-hole pairs are created across the p-n-junction at the heated end, and will absorb heat. The electrons will flow away from this conducting junction in the n-type material, and holes will flow away from it in the p-type material [6]. This process is shown in Figure 1. The equation for the potential difference, ΔV , is given by,

$$\Delta V = \int_{T_0}^T SdT \quad (1)$$

where, S is the Seebeck coefficient, and T is temperature [5]. Additionally, another factor that increases the magnitude of the Seebeck Effect [5], namely the magnitude of the Seebeck coefficient, is known as phonon drag. A net phonon flux exists between the hot and cold regions, where phonons collide with electrons or holes, scattering the electrons towards the cold region. This phonon flux can drag carriers toward the cold side and increase the magnitudes of the Seebeck coefficient in both the n- and p-type materials.

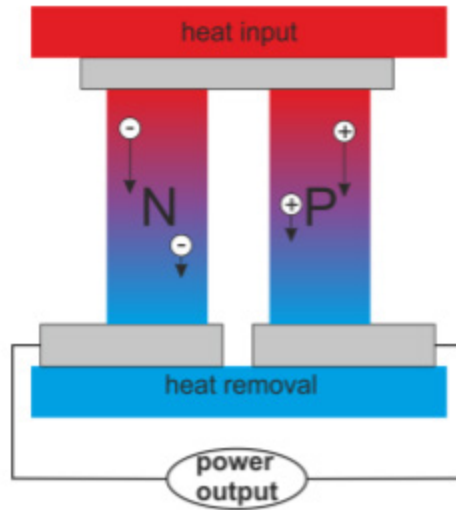


Figure 1. Illustration of the Seebeck Effect in a thermoelectric generator (TEG). Source: [6].

However, the power output of a single TEG [4] is very low. Therefore, multiple TEGs are connected, usually in series, in a thermoelectric module, also known as a thermochain. Figure 2 displays how a thermoelectric module is arranged.

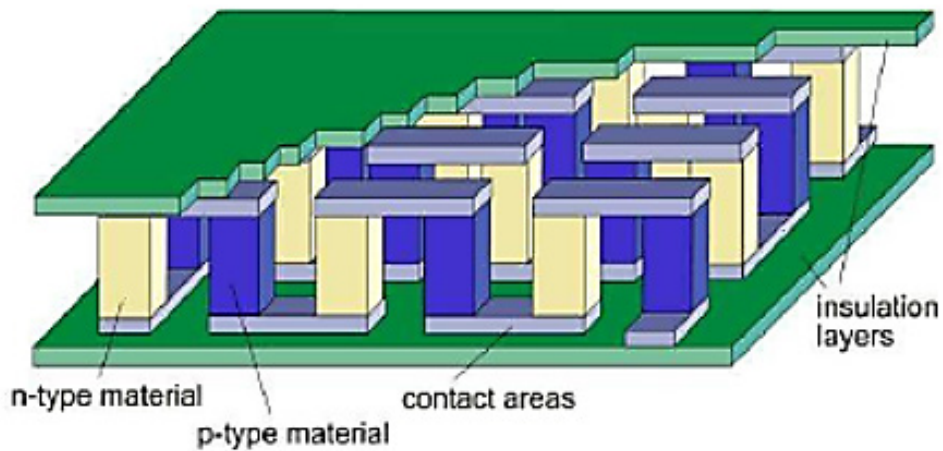


Figure 2. Internal schematic of a thermoelectric generator (TEG) module. Source: [4].

The TEG modules used in these experiments [7] are commercial-off-the-shelf (COTS) products from TEGpro. The model used is a TE-MOD-22W7V-56, which is a 22 W, 7 V module. These modules use bismuth telluride (Bi_2Te_3) [8] as the thermoelectric material. An image of one such module is shown in Figure 3.



Figure 3. TEG module model TE-MOD-22W7V-56.
Source: [8].

C. PREVIOUS RESEARCH PERFORMED USING TEGS

Using TEGs as a means of waste heat energy harvesting have been examined for both commercial and military applications. In this section, samples of industrial and military research that has been performed using this technology have been selected. The first section pertains to research performed by the automotive industry. The second section is about research conducted in a military application.

1. Automotive Research

In 1994, Hi-Z Technology [9], in association with the Department of Energy (DOE) and the California Energy Commission (CEC), experimented with using TEG modules to harvest wasted heat energy from the exhaust of a diesel engine. A hollow, cylindrical heat sink was attached to a 14 L Cummins diesel engine. The inside of the heat sink had fins

that protruded inward, aiding in transferring heat from the exhaust gases. The outside of the heat sink was lined by 72 TEG modules, which were water-cooled. Inside of this contraption, a center body with fins distributed the exhaust gases to flow closer to the inside of the heat sink's walls. They eventually discovered designing the fins to create a swirling flow for the exhaust provided the best results. In their final laboratory experiment, using the fins that produced the swirling flow, they were able to recover 1,068 W while operating the engine at 300 h.p. and 1,700 RPM.

In 2011, one study by Bataar and Kim [10] replaced the conventional radiator of a car with a prototype radiator that incorporated TEG modules. This prototype radiator still cycled coolant water to and from the engine block using the car's existing water pump, thereby eliminating the need to add new cooling equipment. Sandwiched between the hot coolant water ducts and passive heat sinks were 72 TEG modules. During their experiments, the prototype yielded a maximum power of 28.5 W at idle conditions, and 75 W while driving 80 km/hr (49.7 mph).

In spite of the progress made by the two aforementioned studies and others besides them, implementing TEG modules on vehicles comes with some drawbacks. In an analysis by Sivaprahasam, Harish, Gopalan, and Sundararajan [11], there are factors preventing this method of waste heat energy recovery from reaching commercialization. When automotive exhaust thermoelectric generators (AETEGs), systems that draw heat from engine exhaust, are built into a vehicle, they introduce certain parasitic losses. Adding the equipment necessary for these AETEGs to function increases the weight of the vehicle, making the engine work a little harder to move the vehicle. Separate water pumps needed to cool the AETEGs require an electrical load on top of the original load. If heat exchangers are inserted into the flow of the exhaust gases, this will negatively influence engine performance, creating a certain amount of back pressure. These losses are not insignificant. For a car with a 1.5 L engine, a power loss of 12 W was experienced for every 1 kg of added equipment.

Perhaps the biggest inhibition [11] holding back the use of TEGs in the automotive industry in general is the cost. For the AETEGs, the cost comes to \$10 for every Watt of energy recovered. Regardless of whether the TEG modules draw the heat energy from the

exhaust or the radiator, special circuitry is needed to integrate the recovered electrical power into the existing circuitry. The power recovered is dependent on the engine duty cycle, causing it to vary widely.

2. Military Application Research

Under a program for the Army Research Lab, RTI International, Creare Inc., and General Dynamics Land Systems partnered to develop a waste heat recovery system [12] using TEGs on a M1 Abrams tank. The prototype was water-cooled by means of pumps, radiators, and fans. Considered to be scaled down, the device was designed to replace part of the tank's engine exhaust duct, using heat exchanging fins to capture some of the exhaust heat.

This prototype was tested [12] on one such tank on a track in Sterling Heights, MI. The results of the test run were promising. A peak power gain of 80.7 W was achieved. By the conclusion of this study, a full-scale design is expected to be developed.

D. REDUCING THE INFRARED SIGNATURE

Linked to this field of study pertains to ways the infrared (IR) signature of military assets can be reduced. While surveillance technology using IR detectors can compromise military units, the biggest threat comes from the weapons that use this form of detection. IR-guided missiles typically home in on the hottest part of the platform, which tends to be the exhaust system or engine [13]. In the case of ships, all other equipment pales in comparison to the IR signature emitted by the exhaust stacks [14].

While the exhaust plume still contributes significantly to the IR signature of a platform [14], one method to reduce the severity of the signature generated by the other components is a method known as optical blocking [13], or masking, of hot engine parts. Optical masking [13] is achieved by covering engine components and the exhaust ducts with something that physically conceals them and helps reduce their IR visibility. In this paper, the effectiveness of using the thermoelectric waste heat harvesting prototype developed by NPS [15] as an optical blocker will be assessed.

II. COMSOL MODEL OF WATER-COOLED THERMOELECTRIC WASTE HEAT HARVESTING PROTOTYPE

The purpose of this chapter is to detail the steps taken to build a model of the prototype [15] in COMSOL Multiphysics and simulate the observed heat transfer interactions. By creating this model, we hope to better understand how the TEG modules are heated on one side and cooled on the other, with the additional hopes to apply this understanding to future models.

A. BUILDING THE MODEL USING THERMAL DATA

In 2019, Howard built a water-cooled thermoelectric waste heat harvesting prototype [15], shown in Figure 4. The prototype includes eight TEG modules that are sandwiched between two aluminum blocks. The base plate is curved to allow close contact onto the muffler of a DuroStar DS4000S portable, gasoline-powered generator. The top plate is a hollow piece that allows internal water circulation, acting as a heat sink. The circulating water is cooled by a Bay Voltex Tempryte, model PT-0212-AC, water chiller with a cooling capacity of 2,800 BTUs. During this project, an initial, generic model was built in COMSOL, but it did not match the built prototype.

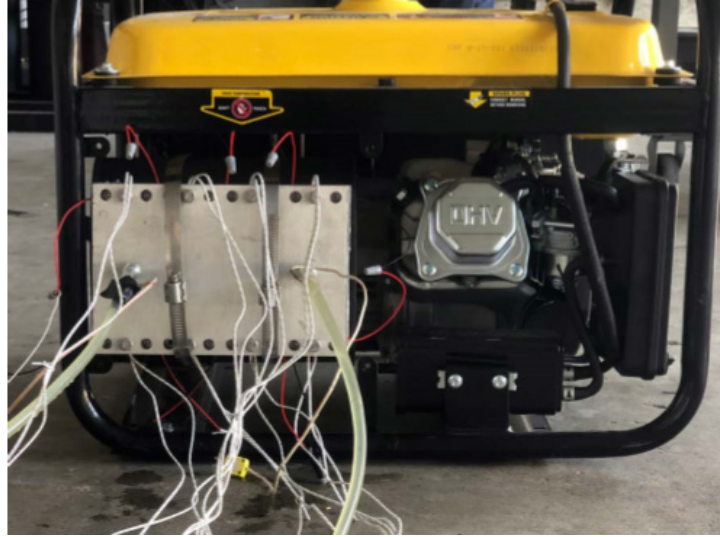


Figure 4. Water-cooled thermoelectric generator waste heat harvesting prototype. Source: [15].

The goal is to transform all aspects of the prototype into a COMSOL model. As if following the flow of the heat transfer, the first step was to recreate the muffler, which is the heat source. An isolated, angled view of the muffler is shown in Figure 5. I measured the muffler's dimension and applied them to an COMSOL object with an oval cross-section, shown in Figure 6.



Figure 5. Isolated view of the muffler. Source: [16].

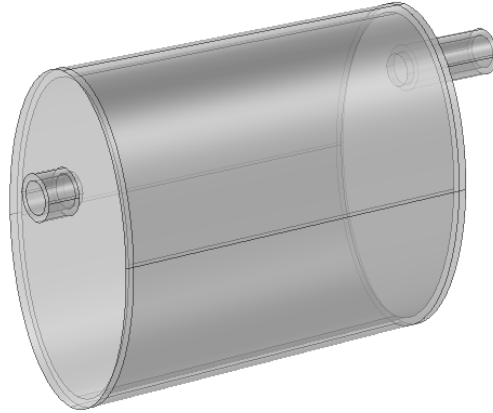


Figure 6. A semi-transparent model of the muffler built in COMSOL

The internal workings of the muffler are not known without physically cutting it open, which would permanently destroy it, without a means to repair it. The muffler was therefore assumed hollow in the model. There is an observable offset between the muffler inlet and outlet pipes, so that was incorporated in the design. The material selected for the muffler was cast iron [16]. The next step was to determine how the exhaust flows through the muffler, and what the initial temperature could be. Using a FLIR camera and ResearchIR software, the mean surface temperature was estimated to be 279°C. The FLIR image with the statistics generated by the ResearchIR software are shown in Figure 7.

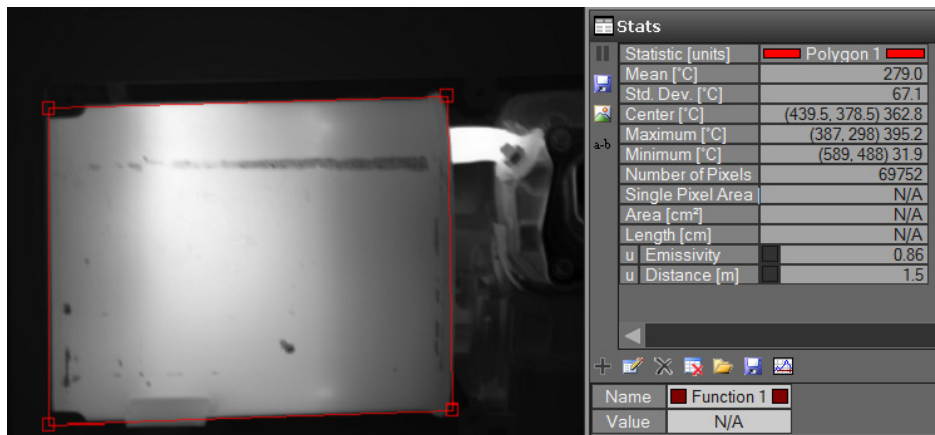


Figure 7. FLIR image of the muffler in ResearchIR, with data given on the mean surface temperature within the region of interest (ROI), shown as a red box

Knowing the mean surface temperature provided an experimental value to attain for my model. The next step was to estimate the flow of the exhaust gases into the muffler. The DuroStar DS4000S gasoline-powered generator [17] has a single cylinder, four-stroke prime mover, with a cylinder volume of 208 cc and a speed of 3600 rpm. A four-stroke engine expels the exhaust gases every second revolution [18], and assuming the volume of the cylinder is the volume of the exhaust gases, we have the following calculation to determine the volumetric flowrate of the exhaust gases into the muffler,

$$3600 \text{ rev/min} \frac{208 \text{ cc}}{2 \text{ rev}} \frac{1 \text{ m}^3}{(100 \text{ cm})^3} \frac{1 \text{ min}}{60 \text{ sec}} = 6.24 \times 10^{-3} \text{ m}^3/\text{s}.$$

The above exhaust gas volumetric flowrate serves as a decent approximation for our model. For simplicity, the exhaust was modeled as “Laminar Flow” in COMSOL. Since engine exhaust is not a material option in COMSOL, and since trying to accurately derive the parameters for it would be very difficult, I assigned air as the material of the gas.

To simulate how the muffler’s heat is lost to the ambient air, I had to account for the convective heat loss (“Heat Flux” in COMSOL) and radiative heat loss (“Surface-to-Ambient Radiation” in COMSOL) by setting the appropriate parameters in the “Heat Transfer in Solids and Fluids” physics in COMSOL. For surface-to-ambient radiation, the emissivity, ε , was needed, along with the ambient air temperature. The ambient air temperature was approximated at 60°F, or about 16°C, which is fairly typical for Monterey, CA, and was close to the temperature when the measurements were being taken. Discussed later in Chapter III, ε for the muffler was measured to be equal to 0.86.

The heat flux was set to convection, which required the convective heat transfer coefficient, h , and the ambient air temperature again. The convective heat transfer coefficient, h , is a function of the boundary layer condition of the object subjected to a fluid or gas, the object’s surface geometry, and a variety of fluid thermodynamic and transport properties [19]. This coefficient is used in the expression for Newton’s law of cooling,

$$q'' = h(T_s - T_\infty) \quad (2)$$

where, q'' is the convective heat flux, T_s is the surface temperature of the object, and T_∞ is the temperature of the ambient fluid [19], which in our case is air. Since the heat flux is not known, I had to take a different approach to solve for h .

Four dimensionless groups were selected to aid in solving for h : the Nusselt number, Nu ; the Grashof number, Gr ; the Prandtl number, Pr ; and the Rayleigh number, Ra . The Nusselt number is the ratio of convection to pure conduction heat transfer [19] and is given in the form of two expressions relevant to this analysis. The first equation for the average Nusselt number, \overline{Nu} , is given by,

$$\overline{Nu} = \frac{\bar{h}L}{k} \quad (3)$$

where, \bar{h} is the average convective heat transfer coefficient, L is the characteristic length, and k is the thermal conductivity of the fluid [19]. By itself, this expression cannot be used to solve for h . However, using a vertical plate approximation, natural convection, and laminar flow of the air, the average Nusselt number can be expressed as,

$$\overline{Nu} = 0.68 + \frac{0.670Ra^{1/4}}{[1+(0.492/Pr)^{9/16}]^{4/9}} \quad Ra \lesssim 10^9 \quad (4)$$

where, Ra is the Rayleigh number and Pr is the Prandtl number [19]. The Prandtl number is the ratio of the momentum and thermal diffusivities [19], and its value can be taken from a table for air. The Rayleigh number represents the magnitude of the buoyancy and viscous forces in the fluid, and is given by,

$$Ra = GrPr \quad (5)$$

where, Gr is the Grashof number [19]. The Grashof number is the measure of the ratio of buoyancy forces to viscous forces, and is given by,

$$Gr = \frac{g\beta(T_s - T_\infty)L^3}{\nu^2} \quad (6)$$

where, g is gravitational acceleration, β is the expansion coefficient, and ν is the kinematic viscosity [19]. The expansion coefficient, β , is given by,

$$\beta = \frac{1}{T_f} \quad (7)$$

where, T_f is the film temperature of the boundary layer, and is the temperature at which the fluid is to be evaluated [19]. The film temperature is given by,

$$T_f = \frac{1}{2}(T_s + T_\infty). \quad (8)$$

In this vertical plate approximation, the characteristic length, L , is the height of my object, which in the first case is the side of the muffler. With the mean surface temperature found in Figure 7, and the ambient air temperature known, the first step was to solve for T_f . Using the film temperature, I used a table for air at atmospheric pressure [19] to find the values for ν , k , and Pr . When performing the calculations for the muffler, I received a value of 420.5 K for T_f , which is between the tabular values for 400 K and 450 K. So I developed regression models for ν , k , and Pr , using data from the table and Microsoft Excel's trend lines, between the temperatures of 100 K and 800 K.

Next, I solved for the Grashof number in Equation 6, and then I was able to solve for the Rayleigh number in Equation 5. I verified the Rayleigh number was still in the laminar region (less than 10^9), and then solved for Equation 4. With the average Nusselt number now known, I was able to solve for \bar{h} in Equation 3, which returned a value of 7.295 W/(m²•K). To make the calculations repeatable, I developed a MATLAB script, which is attached in Appendix A.

With all of the other parameters estimated, I was able to go back and adjust the inflow temperature into the muffler model in COMSOL to achieve the observed mean surface temperature. To determine the average surface temperature generated by the model, I selected the surfaces that would be facing the camera. After running a parametric sweep and fine-tuning the value, with a "Normal" mesh size in COMSOL, I found the muffler inlet temperature that gave a surface average of 282.1°C to be 600°C, which is very close to the observed value.

The temperature profile from the heat test conducted on the muffler is shown in Figure 8. The hottest region is the surface area near the outlet pipe. That is because the exhaust flows directly through the hollow cavity and impacts the inner wall above the outlet pipe. However, as seen in the FLIR thermal image in Figure 9, the hottest region of the real muffler is in the middle. The image indicates at least two internal baffles. Efforts to recreate

this effect without knowing the internal workings failed. Still, the average surface temperature of the hollow muffler model matches with that was determined earlier.

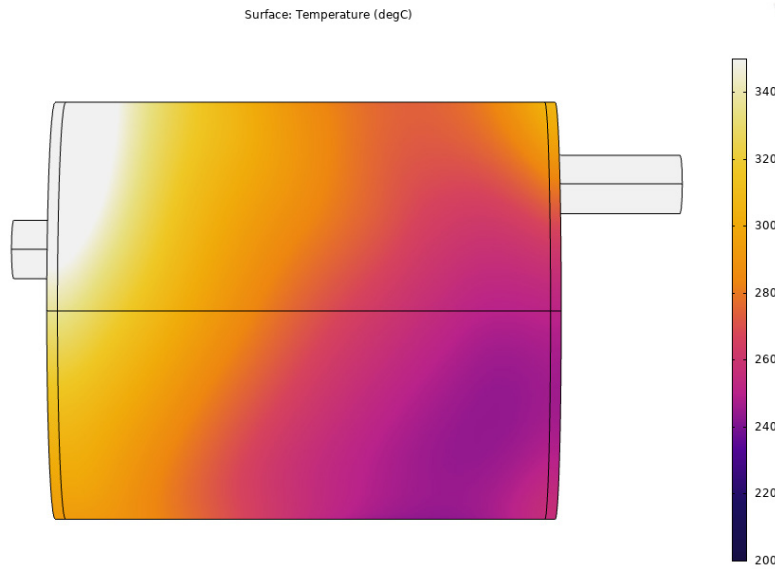


Figure 8. Temperature profile of the muffler model in COMSOL

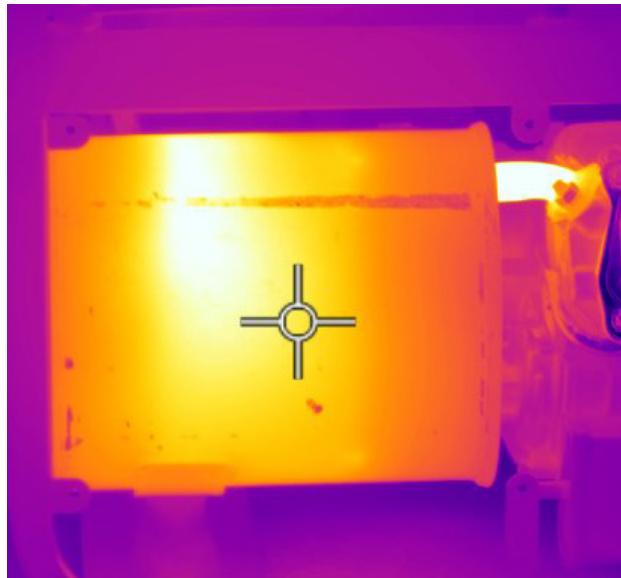


Figure 9. FLIR image of the muffler

The second piece of geometry to build was the aluminum base plate upon which the TEG modules are heated. I created a rectangular block and cut out the grooves that were made for the thermocouples. To ensure proper contact, I overlapped the base plate and the muffler, created an intersection, and removed the inner section of the block. The finished product at this stage is shown in Figure 10. Since the bolt holes are filled when the assembly is put together, one simplification was to not add the holes in the base plate.

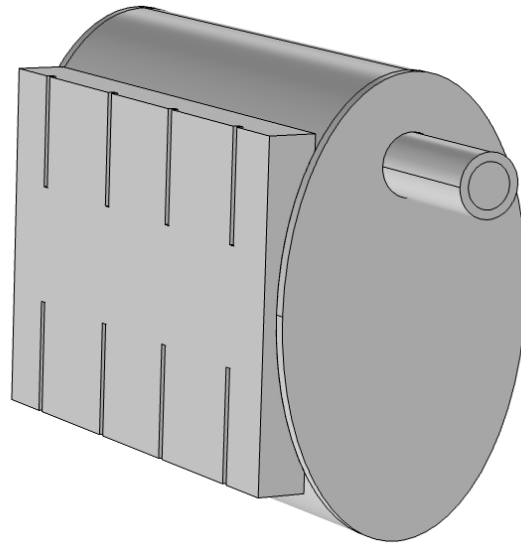


Figure 10. Model of the muffler and base plate built in COMSOL

Next, I needed to add the TEG modules. Thanks to my predecessors [20], I had two choices available to me: one TEG module model with highly detailed thermochains inside, and a simplified version that allowed for a quicker computation time. The simplified design collapses the inner workings into a single block, instead of the zigzagging thermochains, yet still maintaining the volume of the inner parts. The simplified TEG module would avoid prohibitively high computational costs when eight of these TEG modules were to be introduced. Both TEG module models are shown in Figures 11 and 12.

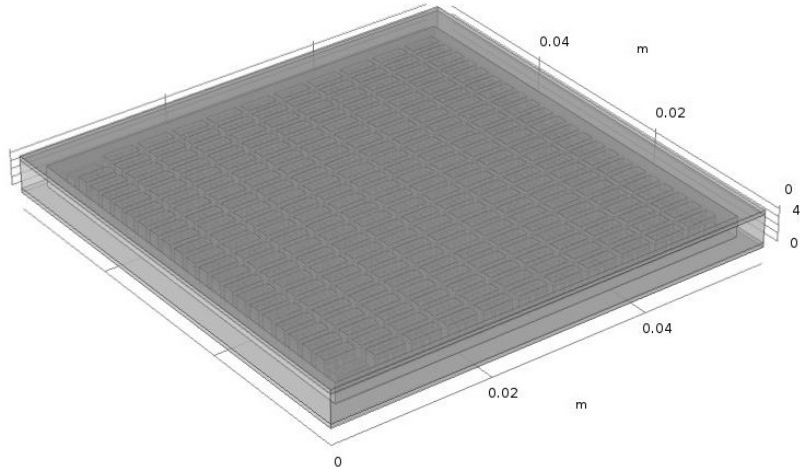


Figure 11. Semi-transparent COMSOL model of the detailed TEG module.
Source: [20].

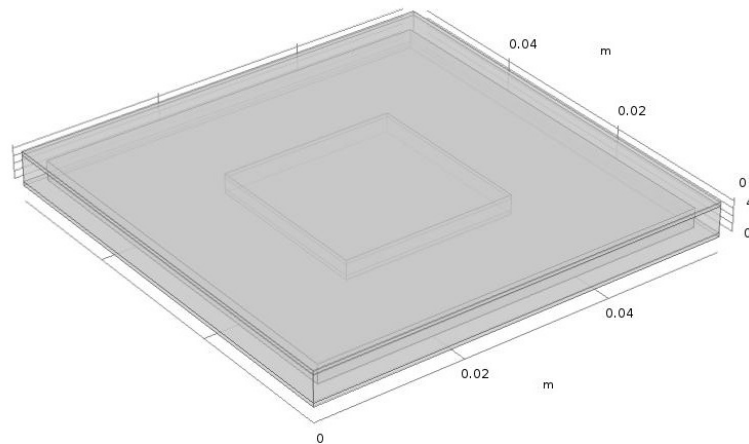


Figure 12. Semi-transparent COMSOL model of the simplified TEG module.
Source: [20].

Before settling on selecting the simplified TEG module model for use in the larger model, I ran an independent heat transfer test on both models to ensure that their thermal behavior is nearly identical, and that using the simplified model would not negatively impact the fidelity of the model. For a proper test, the materials needed to be assigned. The top and bottom layers are graphite [8]. Since graphite was not included in the material

library for our version of COMSOL, the necessary information was inputted manually from a material table [19], giving the following values: density, ρ , of 2210 kg/m³, specific heat at constant pressure, c_p , of 709 J/(kg•K), and thermal conductivity, k , of 1950 W/(m•K).

Inside of the graphite layers and sealing the edges is a ceramic material [21]. However, the type of ceramic was never specified, so I tested five different forms of ceramics: silicon, alumina, dense zircon-based porcelain [22], silicon carbide [19], and silicon nitride [19]. Silicon and alumina are available in COMSOL, but porcelain, silicon carbide, and silicon nitride are not. Those material properties had to be entered manually, as with the graphite. Later, once the model was completed, each ceramic was used and the differential temperatures they provided were recorded.

Whether it is the simplified model with a single block, or the detailed model with the thermochains, they are comprised of three layers. The innermost layer is the thermoelectric material consisting of bismuth telluride (Bi_2Te_3), and the top and bottom layers are the aluminum electric contacts [20]. The inner empty space surrounding the inner block was assumed to be air.

A heated block was placed directly underneath each TEG module. The same arbitrary values for the convective heat transfer coefficient and emissivity were given to both. Using the different ceramics, the average surface temperature difference between the two models varied from 0.07 K to 0.5 K. Therefore, I selected the simplified TEG module model moving forward. I arranged the TEGs on the base plate in a two-by-four pattern as they are in the prototype, shown in Figure 13.

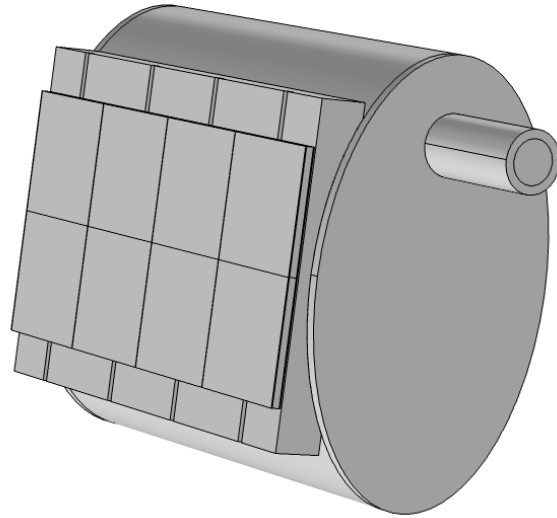


Figure 13. COMSOL model of simplified TEG modules on the base plate, which is attached to the muffler

The last component to develop is the water cooler. This component is comprised of two blocks: the lower block with the water channels carved within it, and the top plate with the inlet and outlet nozzles. I started with the lower block and designed the grooves that were used for thermocouples. Next, I opened up the cooler and examined the water channels, which are shown in Figure 14.



Figure 14. Water channels inside of the water cooler

Using a face parallel work plane, I recreated the design and extruded the empty space into the block. The top plate was designed next and affixed on top of the bottom plate. Figure 15 shows a semi-transparent image of the water cooler model.

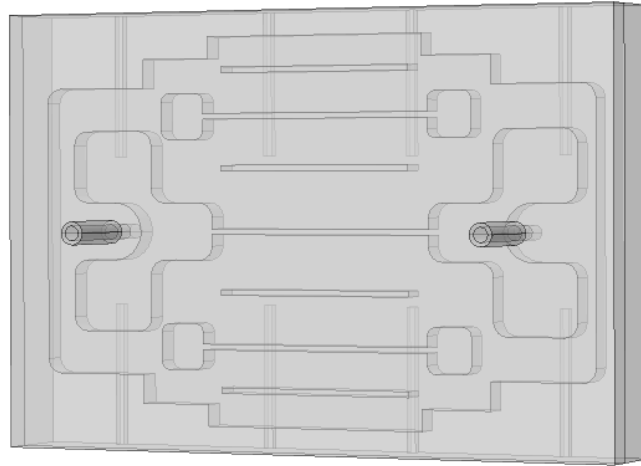


Figure 15. Semi-transparent COMSOL model of the water cooler

To finish the complete model, the final step was to place the water cooler on top of the TEG modules. The finished model is shown in Figure 16, with a comparison to the real prototype shown in Figure 17.

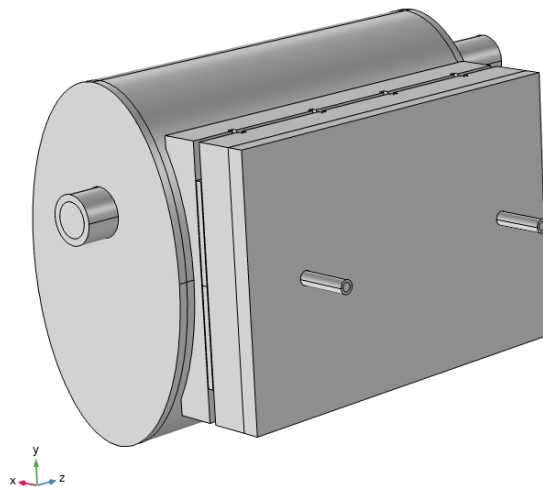


Figure 16. Final COMSOL model of the water-cooled prototype

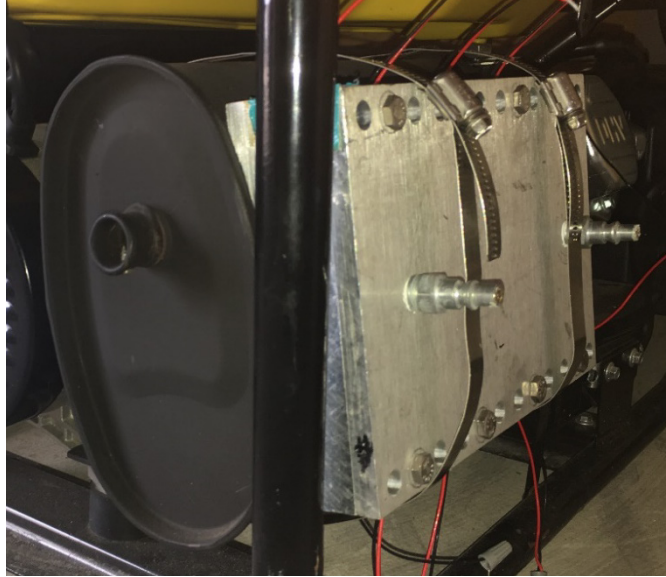


Figure 17. Water-cooled prototype

To be able to run the simulation effectively, the inlet water flowrate and temperature needed to be determined. Initially, the goal was to make the mean surface temperature to be 43.6°C , which was obtained via the FLIR camera and ResearchIR software. However, this value seemed rather high. So the goal became 36°C , which had been measured by a thermocouple when the emissivity was being determined, as discussed in Chapter III. The water is supplied to the water cooling block by means of a Bay Voltex Tempryte, model PT-0212-AC, water chiller. However, product information for this specific water chiller could not be obtained, so the input values needed to be approximated. Having worked with the water chiller in associated experiments, the flowrate is very low, so I approximated it to be 1 gallon per minute, which translates to $6.31 \times 10^{-5} \text{ m}^3/\text{s}$.

I performed the same calculations to find the convective heat transfer coefficient for the water cooler and determined it to be $4.96 \text{ W}/(\text{m}^2 \cdot \text{K})$. The emissivity for the water cooler's surface, also described in Chapter III, was determined to be 0.49. After running simulations, the inlet temperature was determined to be 33°C to give a surface temperature of 36°C . For a water chiller, 33°C does not seem very cool. A likely explanation for this temperature will be addressed in the next section.

B. RESULTS AND ANALYSIS

Before settling on a final solution to the model, I compiled the temperature data using each form of ceramic inside of the TEG modules. To get the best results, I took the maximum temperature of the hot side of each TEG module, and the minimum temperature of the cool side. Based on experimental data [15], the goal is to get an average differential temperature of 60.5°C. Table 1 shows the average differential temperatures when using each type of selected ceramic.

Table 1. Average differential temperatures from the COMSOL model when using different ceramic materials inside of the TEG modules

Ceramic	Average Differential Temperature
Silicon	13.7°C
Alumina	34.9°C
Porcelain	76.6°C
Silicon Carbide	7.8°C
Silicon Nitride	47.9°C

The two materials that give the closest average differential temperatures to our goal are porcelain, which is 16.1°C above the goal, and silicon nitride, which is 12.6°C below the goal. Since silicon nitride is the closest, that is the ceramic material selected for the final model. From here, a solution for the heat transfer model in COMSOL that matches with experimentally observed conditions was obtained.

1. Model Using the Thermal Data

The temperature profile for the heat transfer simulation is shown in Figure 18. When compared to the FLIR image of the real water-cooled prototype in action, Figure 19, there are marked differences. For the COMSOL model, there is a noticeable temperature gradient in the muffler around the TEG assembly, whereas there is a very sharp contrast in the temperature regions in the FLIR image. Some explanations pertain to the internal baffles and possibly greater volumetric inflow for the real muffler.

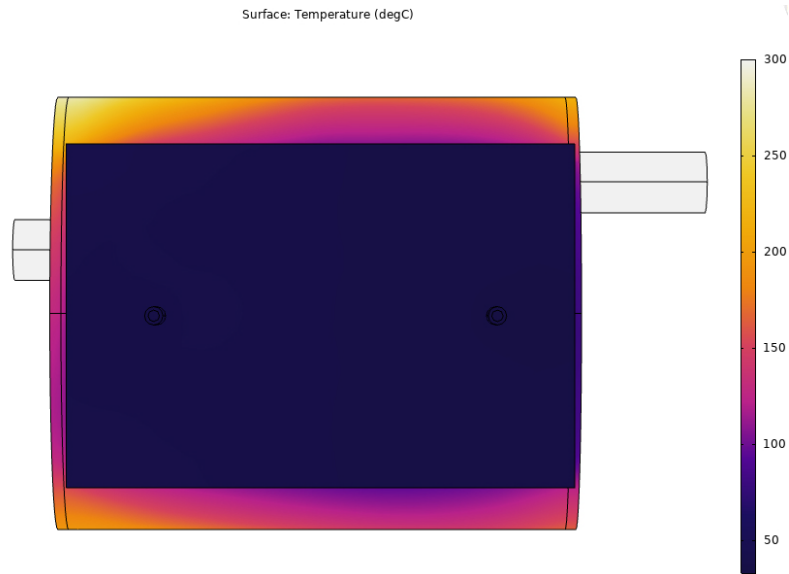


Figure 18. Temperature profile from simulation performed on the final model in COMSOL



Figure 19. FLIR image of water-cooled prototype

To assess the effectiveness of this model, I needed to compare my results with what had been done experimentally [15] before. The temperature measurements for the hot sides

and cool sides of the TEG modules, along with the resulting differential temperatures are given in Table 2.

Table 2. Average experimental temperature measurements on TEG modules operating in prototype assembly. Source: [15].

TEG Module	T_{hot} (°C)	T_{cool} (°C)	ΔT (°C)
1	74.42	17.56	53.86 ± 1.45
2	81.52	20.20	61.32 ± 0.40
3	89.08	22.64	66.44 ± 2.23
4	88.42	22.06	66.36 ± 3.36
5	70.34	19.10	51.24 ± 2.25
6	76.20	18.26	57.94 ± 3.03
7	84.58	20.20	64.38 ± 2.03
8	83.38	20.86	62.52 ± 2.04

As seen in Table 2, the cool side temperatures are much lower than what I had measured experimentally with a thermocouple. In fact, the cool side values from Howard’s data [15] are 19.2°C cooler on average than the values derived from the COMSOL simulation. A possible explanation could be that the water chiller is losing efficiency and may need to have the refrigerant recharged. Due to time and resource constraints as a result of the COVID-19 pandemic, repairs to or replacement of the water chiller will have to wait to a more suitable time. For the moment, we will assess how the model performs using the data that had been gathered in this experiment.

Under “Derived Values” in the “Results” section of the COMSOL model, I took the maximum surface temperature on the hot side of the TEG modules, and then the minimum surface temperature on the cool side. These values, along with the resulting differential temperatures, are given in Table 3. Assuming the same numbering system is being used for the TEG modules for both the experimental [15] and COMSOL simulation values, they are numbered from left to right, with 1 through 4 on the top row, and 5 through 8 on the bottom row.

Table 3. Temperature measurements on TEG modules derived from COSMOL model

TEG Module	T_{hot} (°C)	T_{cool} (°C)	ΔT (°C)
1	110.36	40.58	69.78
2	91.94	40.65	51.29
3	79.74	38.11	41.63
4	83.48	36.17	47.31
5	94.9	39.95	54.95
6	81.80	40.03	41.77
7	73.53	37.76	35.77
8	76.89	36.17	40.72

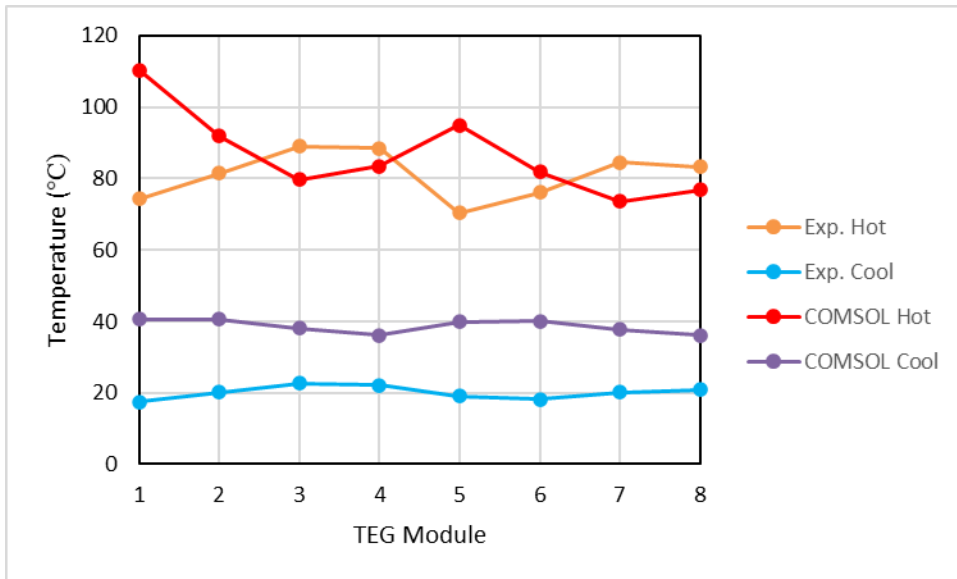


Figure 20. Graphical representation of the hot side and cool side data for both the experimental and COMSOL simulation temperature readings

As seen in Figure 20, the hot side temperatures data points are closer, yet they seem to mirror each other. This behavior is also seen with the differential temperatures in Figure 21. The temperature differences are greater for the experimental data toward the right half of the muffler, TEG modules 3, 4, 7, and 8. Whereas in the simulation, the

temperature differences are greater toward the left half of the muffler, TEG modules 1, 2, and 5. This can be attributed to the fact the COMSOL model of the muffler is hollow, allowing the exhaust to impact the left side wall, heating up that section the most. In the real muffler, there are most likely baffles inside to interrupt and redirect the flow. Without tearing open the muffler, the internal design cannot be known with the tools presently available.

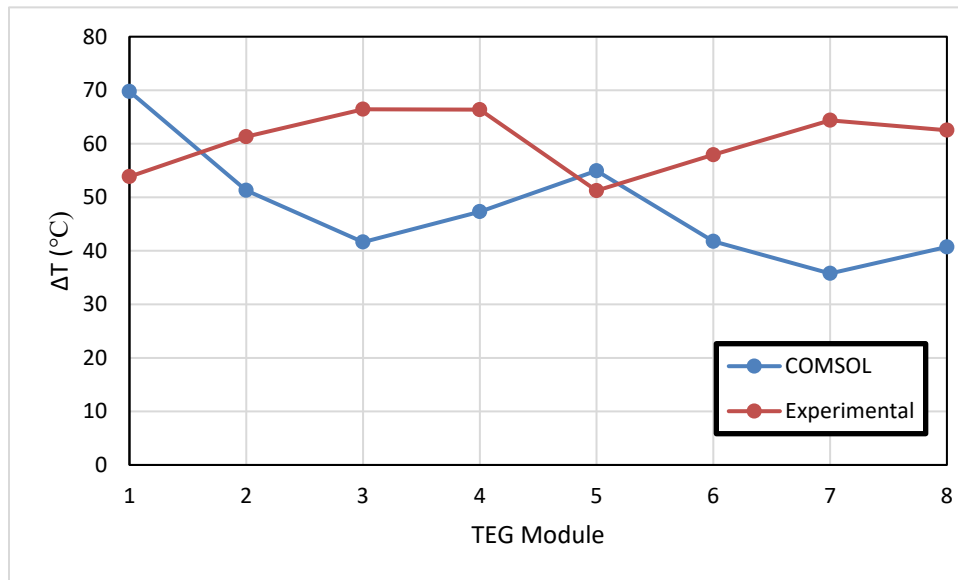


Figure 21. Differential temperatures plotted for each TEG module for both the experimental and COMSOL values

The next step is to see what sort of electrical power the TEG modules in this simulation could theoretically provide. Howard [15] had taken several voltage and current readings over the course of her experiments. The TEG modules were wired in series with each other and also with a load resistor, R_{load} . The average voltage and current readings, along with the associated power, are given in Table 4.

Table 4. Average experimental voltage and current readings across a load resistor, generated by the water-cooled prototype, with resulting power. Source: [15].

$R_{load} (\Omega)$	$V_{load} (V)$	$I_{load} (A)$	Power (W)
1.00	0.471 ± 0.043	0.481 ± 0.028	0.226 ± 0.033
10.00	3.002 ± 0.187	0.304 ± 0.021	0.913 ± 0.120
20.00	4.658 ± 0.248	0.233 ± 0.010	1.084 ± 0.102
33.00	5.874 ± 0.235	0.180 ± 0.009	1.058 ± 0.090
47.00	6.640 ± 0.352	0.141 ± 0.007	0.936 ± 0.094
55.00	6.842 ± 0.367	0.135 ± 0.006	0.926 ± 0.087

Howard [15] had also performed experiments to characterize the performance of a TEG module. This characterization test was performed on a single TEG module at a time on a hot plate. Equations 9 and 10 below show the open-circuit voltage, V_{oc} , and the internal equivalent resistance, R_{eq} , for a TEG module as a function of a temperature difference, T_{diff} .

$$V_{oc} = 0.0187T_{diff} - 0.0051 \quad (9)$$

$$R_{eq} = 0.0078T_{diff} + 2.1829 \quad (10)$$

Each TEG module can be modeled as a battery with internal resistance. In an attempt to replicate the experimental measurements, I calculated the individual open-circuit voltages and internal resistances based on each TEG module's differential temperature. Treating them to be wired in series with a load resistor, Kirchhoff's loop rule [23] yields Equation 11.

$$\sum V = 0 = V_{oc-TEG1} - IR_{eq-TEG1} + \dots + V_{oc-TEG8} - IR_{eq-TEG8} - IR_{load} \quad (11)$$

From Equation 11, the load current, I_{load} , can be solved as shown in Equation 12.

$$I_{load} = I = \frac{\sum_{i=1}^8 V_{oci}}{R_{load} + \sum_{i=1}^8 R_{eqi}} \quad (12)$$

Across the load resistor, the load voltage can be calculated via Ohm's Law [23] in Equation 13, and the power can be calculated [23] as shown in Equation 14.

$$V_{load} = I_{load}R_{load} \quad (13)$$

$$P = I_{load}V_{load} \quad (14)$$

In this process, it is seen that the placement of the TEG modules does not come into play, so long as they are wired in series. The open-circuit voltages generated and the internal resistances imposed by each TEG module are solely a result on the differential temperature for each module. Rearranging the experimental data and the simulation values for the differential temperatures at each TEG module from lowest to highest, the results are plotted in Figure 22. Since all but one of the differential temperature values for the simulation fall below those of the experimental data, we can expect the overall performance of the COMSOL model to be less than that determined experimentally.

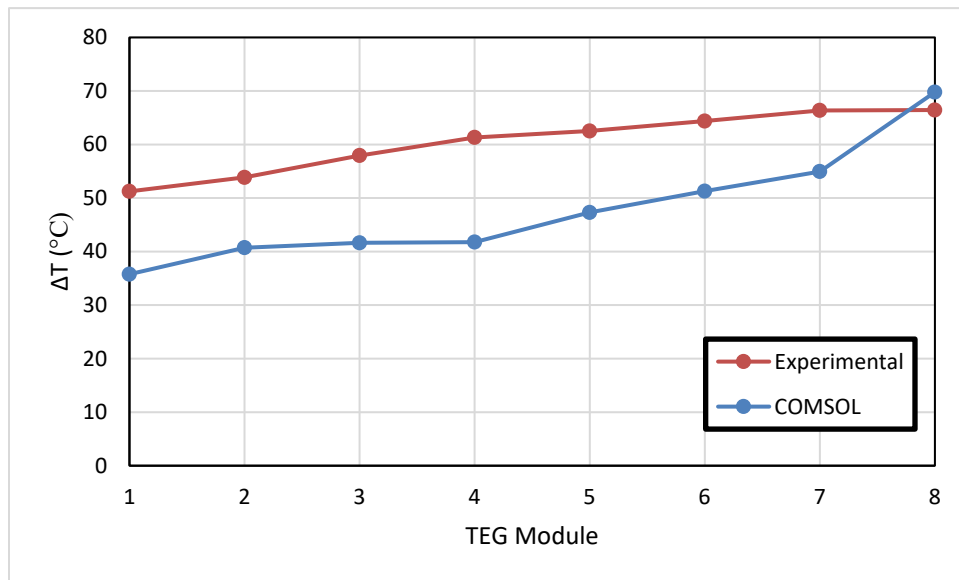


Figure 22. Differential temperature for the experimental data and the simulation values arranged from lowest highest

Using Equations 9 through 14, and using the same load resistance values from the experiment, the theoretical values for voltage, current, and power, derived from the simulated differential temperatures, are given in Table 5. As an additional comparison, I used the same equations with the experimentally measure temperature differences, which serves as the theoretical prediction for current, voltage, and power. The differences

between the experimental, theoretical, and COMSOL model values are shown graphically in Figures 23, 24, and 25.

Table 5. Theoretical voltage, current, and power values across a load resistor, derived from TEG module open circuit voltage and internal resistance equations, as a function of differential temperatures obtained from COSMOL model

$R_{load} (\Omega)$	$V_{load} (V)$	$I_{load} (A)$	Power (W)
1.00	0.332	0.332	0.110
10.00	2.340	0.234	0.547
20.00	3.523	0.176	0.621
33.00	4.399	0.133	0.586
47.00	4.965	0.106	0.524
55.00	5.194	0.094	0.490

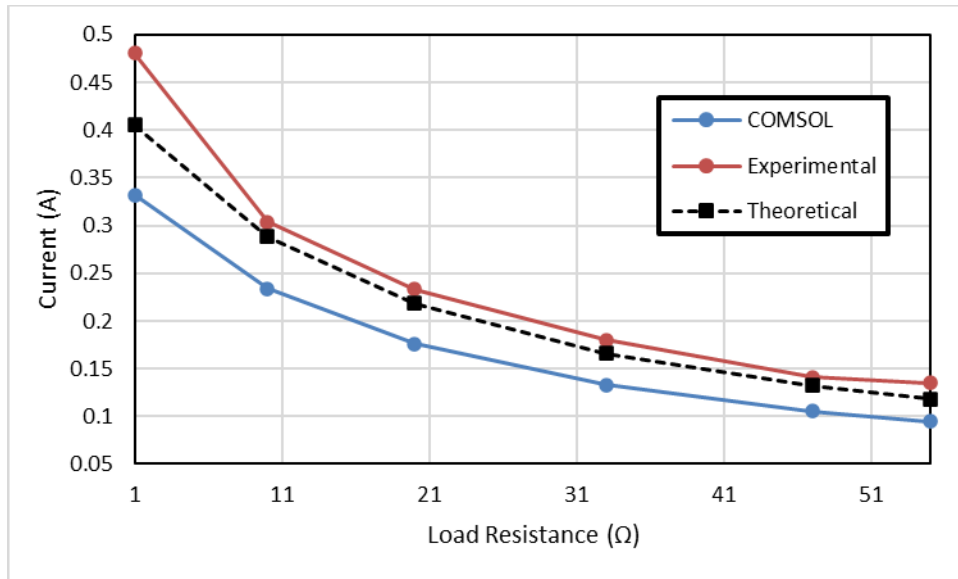


Figure 23. Current vs. load resistance for the average experimental values, theoretical values using the experimental differential temperatures, and the COMSOL model's theoretical values

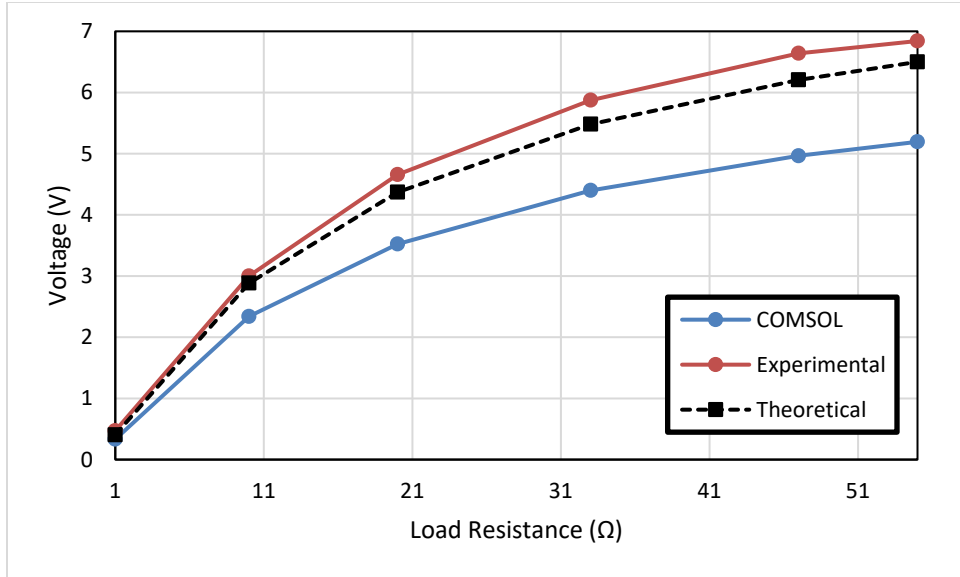


Figure 24. Voltage vs. load resistance for the average experimental values, theoretical values using the experimental differential temperatures, and the COMSOL model's theoretical values

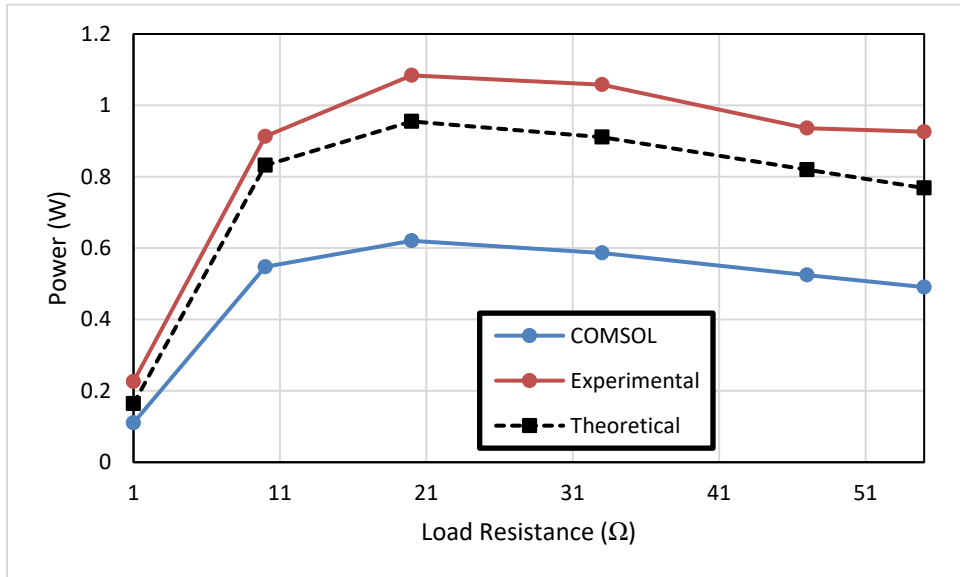


Figure 25. Power vs. load resistance for the average experimental values, theoretical values using the experimental differential temperatures, and the COMSOL model's theoretical values

In all cases, the COMSOL model values for current, voltage, and power lagged behind the experimental and theoretical values, but still exhibited similar trends. The lower performance is as expected. Even the prototype's theoretical values were less than the experimental values. This is likely due to the fact Equations 9 and 10 were developed by characterizing the performance of a single TEG module by itself [15]. Also, placing the TEG modules directly next to each other changes the thermal configuration (there is less heat loss especially for the TEG modules in the middle), and hence their performance.

The COMSOL model's theoretical current values displayed the constant divergence from the experimental and theoretical values for all load resistances. However, the voltage and power values diverged more with increased load resistances. Therefore, it is likely that this approximation for temperature differences recorded in the COMSOL simulation are better for load resistances of 10 Ω or less.

2. Adjusting the Model to Match Experimental Data

In order to refine the model to replicate what was observed experimentally by Howard [15] (where the TEG modules and the water cooler were operating closer to their specifications), the inputs of the model were adjusted iteratively until the average temperature values closely resembled the data. The heat transfer coefficients and emissivities from all surfaces were kept constant. After several simulations, the final result is given in Table 6. To achieve this, the exhaust inflow temperature and volumetric flow rate were increased to 630°C and 7.00 X 10⁻³ m³/s respectively, and the water inflow temperature was decreased to 13°C. This new water inflow temperature seems realistic for a properly functioning water chiller.

Table 6. Temperature measurements on TEG modules derived from the adjusted COSMOL model

TEG Module	T_{hot} (°C)	T_{cool} (°C)	ΔT (°C)
1	105.47	22.21	83.26
2	83.65	22.40	61.25
3	69.26	19.25	50.01
4	73.49	16.76	56.73
5	87.13	21.51	65.62
6	71.88	21.67	50.22
7	62.15	18.86	43.29
8	66.51	16.77	49.75

The temperature data are plotted in Figure 26. Both the hot and cool side temperatures mirror the respective data. However, the cool side temperatures are much closer than the hot side values. In Figure 27, the differential temperatures are again arranged from the lowest to the highest values for both the experimental and simulated data. While it is not a perfect match, it is certainly closer than the earlier model.

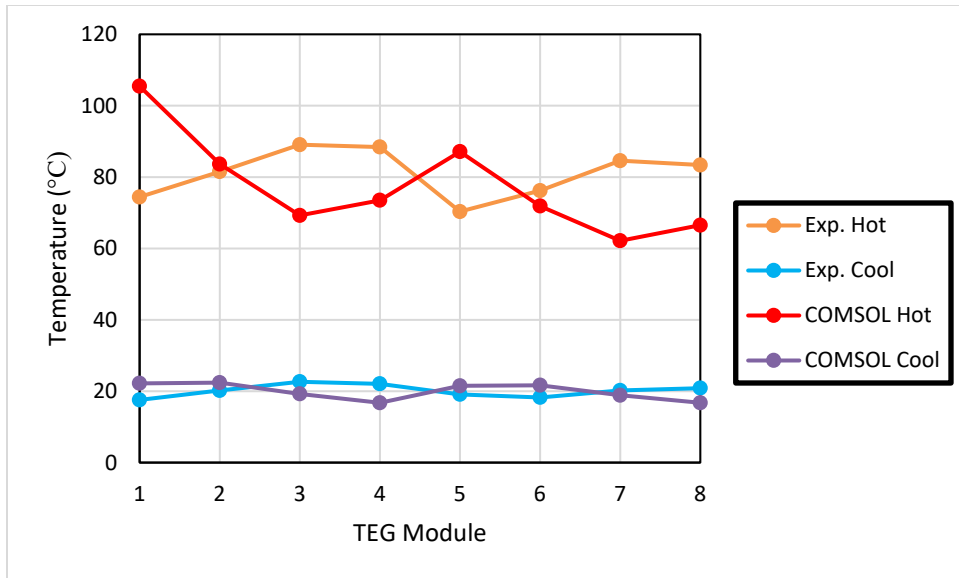


Figure 26. Graphical representation of the hot side and cool side data for both the experimental and the adjusted COMSOL simulation temperature readings

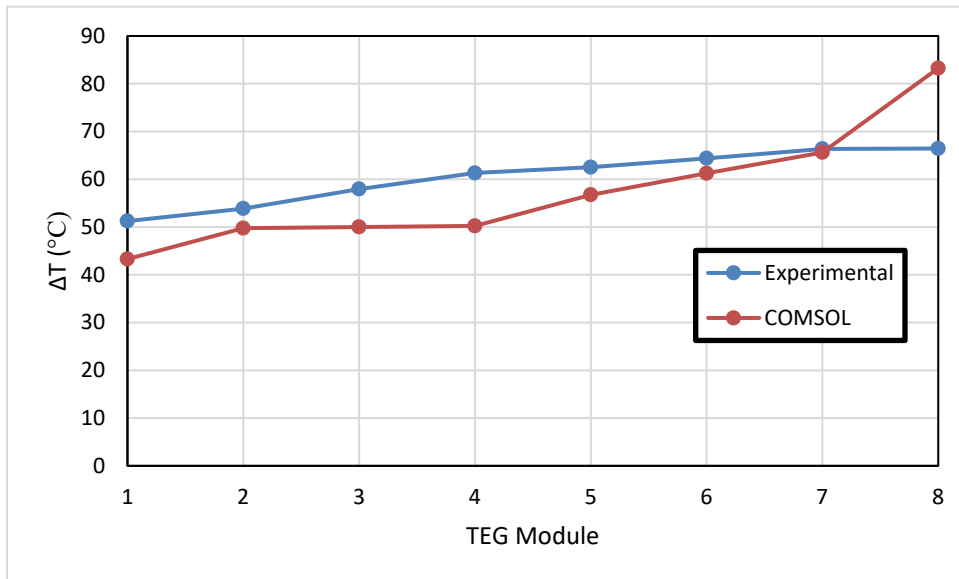


Figure 27. Differential temperature for the experimental data and the adjusted simulation values arranged from lowest highest

With the differential temperatures known, I repeated the calculations for the current, voltage, and power as before. The theoretical results for the COMSOL model are tabulated in Table 7. From this, the current, voltage, and power are plotted against the experimental and theoretical values in Figures 28, 29, and 30.

Table 7. Theoretical voltage, current, and power values across a load resistor, derived from TEG module open circuit voltage and internal resistance equations, as a function of differential temperatures obtained from the adjusted COSMOL model

$R_{load} (\Omega)$	$V_{load} (V)$	$I_{load} (A)$	Power (W)
1.00	0.388	0.388	0.151
10.00	2.758	0.276	0.761
20.00	4.172	0.209	0.870
33.00	5.228	0.158	0.828
47.00	5.914	0.126	0.744
55.00	6.193	0.113	0.697

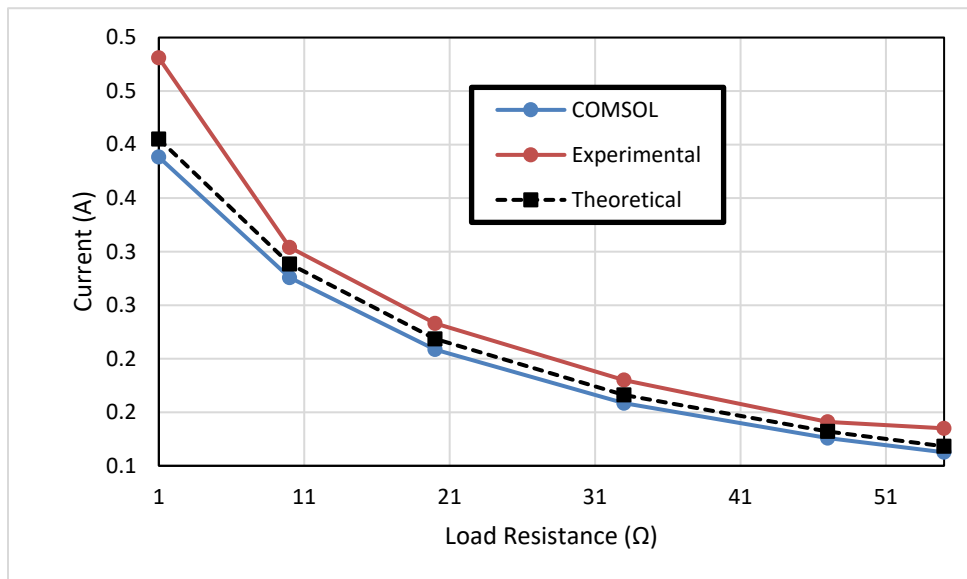


Figure 28. Current vs. load resistance for the average experimental values, theoretical values using the experimental differential temperatures, and the adjusted COMSOL model's theoretical values

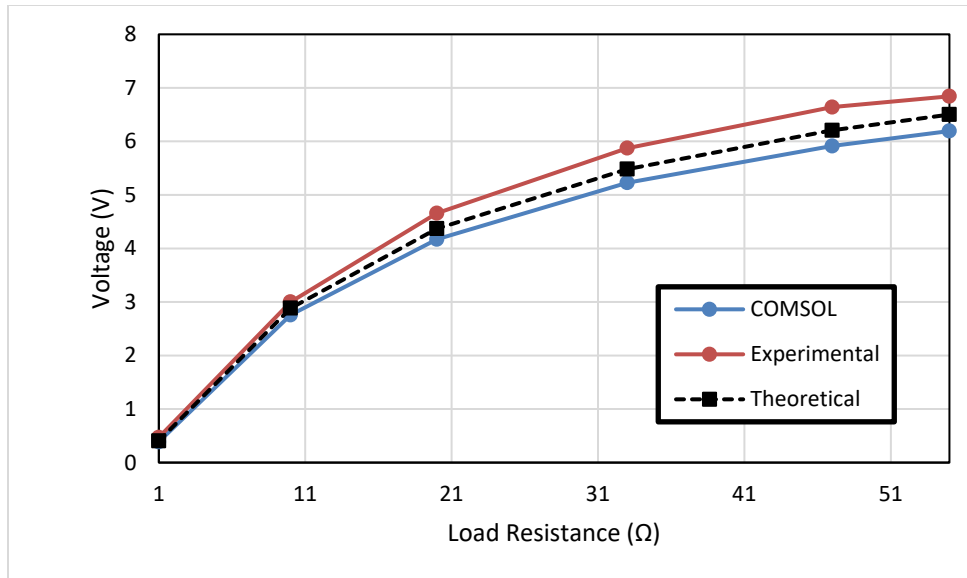


Figure 29. Voltage vs. load resistance for the average experimental values, theoretical values using the experimental differential temperatures, and the adjusted COMSOL model's theoretical values

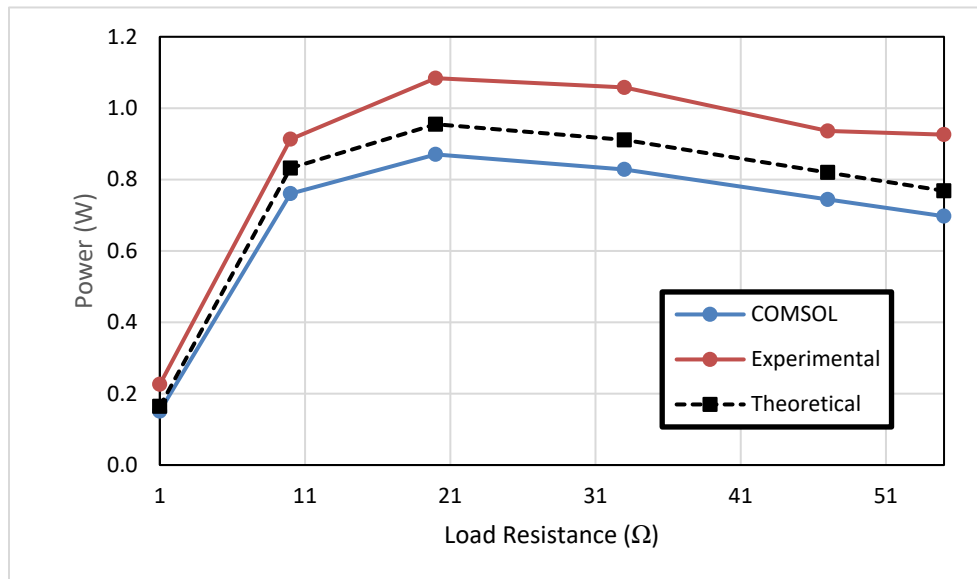


Figure 30. Power vs. load resistance for the average experimental values, theoretical values using the experimental differential temperatures, and the adjusted COMSOL model's theoretical values

In Figure 28, the COMSOL model's theoretical current plot is the closest to the prototype's theoretical values, and very close to the experimental values, particularly between 10 Ω and 47 Ω . In Figure 29, the COMSOL model's theoretical voltage is nearly identical to the prototype's theoretical values, and shows even minor divergence from the experimental values beginning around 20 Ω . Because of the diverging values for voltage, the COMSOL model's theoretical power diverges the most from the experimental power values beginning at 20 Ω also, which is seen in Figure 30. Still, the COMSOL model's theoretical power closely matches the prototype's theoretical values. In all three plots, the COMSOL model's theoretical values exhibit the same trends as those of the experimental and theoretical data. Again, this approximation appears to work best at load resistances of 10 Ω or less. A comprehensive list of the parameters entered into the COMSOL model is provided in Appendix C.

III. ASSESSING THERMAL RADIANCE REDUCTION OF THE THERMOELECTRIC WASTE HEAT HARVESTING PROTOTYPE

In this section, I will discuss the steps I took to analyze how the TEG assembly attached to the muffler affects the radiant power detected by an IR sensor at some distance. The purpose of this effort is to study how much more difficult it would be for an IR sensor to detect the exhaust system of a platform using this or similar TEG assemblies. Reducing how visible the platform is in the IR spectrum could be advantageous against an adversary's surveillance or weapon systems.

A. DATA COLLECTION METHOD

The IR sensor used to collect my data was a Forward Looking Infrared (FLIR) model T1030sc thermal camera. The exhaust system analyzed was a DuroStar model DS4000S gasoline-powered generator. Three configurations were studied: the muffler with no attachment; the TEG assembly attached and with water running through the cooler; and the TEG assembly attached and with no water running through the cooler. The third configuration listed, the TEG assembly attached with no water running through the cooler, is to serve as a comparison.

1. Thermal Imaging and Emissivity Estimates

Thermal images taken by the FLIR camera can be analyzed in detail by the ResearchIR software [24]. This software can study images in two modes: temperature and radiance. My focus here was on radiance. To obtain accurate radiance data, I needed to determine the approximate emissivity of the metal objects photographed.

Radiance [25] is the measure of radiant flux, or radiant power, emitted by a source per unit solid angle and per area of the source. Emissivity [19] is the radiative property of a surface. Dependent on the surface material and finish, emissivity gives a measure on how efficiently a surface emits energy relative to a blackbody; it ranges in value from 0 to 1.

I needed to determine the approximate emissivity of the muffler and the TEG assembly. Due to schedule constraints and time required for the exhaust system to cool in

between making configuration changes, I performed the data collection on two separate days, with the muffler without the TEG assembly on the first day, and the TEG assembly attached on the second day, both with and without water flowing through the cooler.

I started the generator and operated it for about 20 minutes, allowing time for the muffler to reach a stable temperature. As the generator warmed up, I set up the FLIR camera roughly 10 ft. (approximately 3 m) from the muffler, measuring the distance with a measuring tape. I connected the FLIR camera to the laptop and controlled the camera through the ResearchIR software. Within this mode, distance and emissivity values can be adjusted by manual override.

Once 20 minutes had elapsed, I used a MDC model BDTC-J-120 thermocouple to take the surface temperature of each object. Muffler vibrations made it difficult to gather stable temperature readings, so I tucked the probe in a grooved section of the muffler's lower area on the side closest to the muffler's exhaust. Once a stable temperature had been reached, I used the screen controls on the ResearchIR software to focus a graphical region of interest (ROI) on the area the thermocouple had measured the temperature. With the ROI in place, I opened the temporal plot of temperature, manually set the distance from the muffler, and adjusted the emissivity until the temporal plot settled around the temperature measured. The data for this step is shown in Table 8.

With emissivity determined for the muffler, I proceeded to use the FLIR camera alone to take photographs at predetermined distances, from 5 ft. to 30 ft. in 5-ft. increments. This distance span worked best for the loading dock area where the generator was operated.

On the second day, I repeated the process for the TEG assembly attached to the muffler, first without water flowing through the cooler. This time I tucked the thermocouple's probe inside the metal band used to secure the assembly. Once a stable temperature was measured, I set the ResearchIR's ROI to focus on the assembly's metal just outside of the metal band, and where the thermocouple's probe had been. Like before, I repeated the steps for approximating the emissivity, and then for taking the thermal images at the same distances. Finally, I took the thermal photographs as before.

Table 8. Temperature measurements and emissivity estimates

Configuration	Temperature	Emissivity, ϵ
Muffler with no attachment	237°C	0.86
TEG assembly without water flowing	73°C	0.46

I analyzed the collected IR images. For each image, I used the ResearchIR software to determine the radiance from the muffler region for each configuration and at each distance for a given configuration. With a single image opened in the software at a time, I placed a ROI over the muffler area and opened the statistics window generated for that ROI. I had used a rectangular ROI for the muffler without an attachment for the first three distances, but switched to a polygonal ROI for all of the rest, to account for the tilt within images. Figure 31 shows a screenshot of one such image with the statistics window using a rectangular ROI. I manually entered the distance at which the photograph was taken, and also adjusted the emissivity value based on the earlier experiments. From this, I recorded the mean radiance from each image, which is recorded in Table 9.

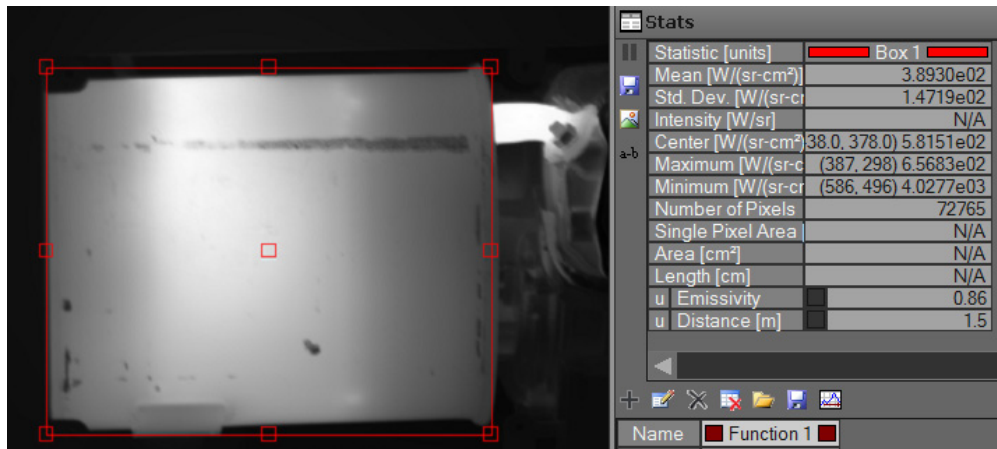


Figure 31. FLIR image of the muffler in ResearchIR software showing the rectangular region of interest (ROI) and window giving the radiance statistics for this ROI.

Table 9. Mean radiance data recorded for the muffler in three different configurations

Distance from Source (ft.)	Mean Radiance [W/(sr•cm ²)]		
	<i>Muffler with no attachments</i>	<i>TEG assembly with no water flowing</i>	<i>TEG assembly with water flowing</i>
5	389.30	156.55	108.88
10	377.56	154.30	110.08
15	356.48	159.79	106.20
20	353.69	158.45	106.95
25	359.13	154.82	111.68
30	359.34	155.97	106.40

2. Radiant Power Estimations

From the reported mean radiance, I needed to calculate the mean radiant power. To do so, I need the reference area over which the thermal radiance is emitted and the solid angle [25]. The reference area is the surface area of the muffler in view. Approximating the side of the muffler as a rectangle, its dimensions are measured at 22.86 cm wide by 20.32 cm tall, for a surface area of 464.5 cm².

The solid angle used is that of a single pixel of the IR detector, receiving the radiant power from the larger sphere surrounding the source at that distance [25]. The solid angle, Ω , is calculated by the approximation,

$$\Omega \approx \frac{A}{r^2} \quad (15)$$

where A is the area of the detector and r is the distance from the source to the detector [26]. In this case, A will be the area of a single pixel. Since pixels are in the form of squares, the area of a pixel can be calculated by squaring the pitch, where the pitch is the pixel spacing [27]. From here, I have the tools needed to translate the mean radiance data into purely mean power detected.

One limitation in my approach for data collection was the short range of distances over which I recorded the images. I needed to predict the values of radiance far beyond the range I had originally selected. Since the radiance values were within 6% difference of each other, I took the mean of the radiance values and used that one value as the fixed radiance detected. The reference area remains constant, leaving the only variable the solid

angle. As seen in Equation 15, the solid angle is inversely proportional to the distance squared.

Since I used the FLIR camera to take the thermal images, I used its detector pitch of $17\ \mu\text{m}$ to get a detector area of $289\ \mu\text{m}^2$. Using Microsoft Excel, I arbitrarily extrapolated the range to 100 m. I then plotted the power detected versus the range from the source for all three cases.

Being able to plot the data in MATLAB was an important later step, so I used Excel to perform a regression analysis. Using a power trend line equation produced the best fit, since power detected is proportional to the inverse of the distance squared. This regression analysis garnered a perfect root mean squared value of 1 for all three plots. The plots of the data, along with the trend line equations and goodness of fit values, are shown in Figures 32, 33, and 34.

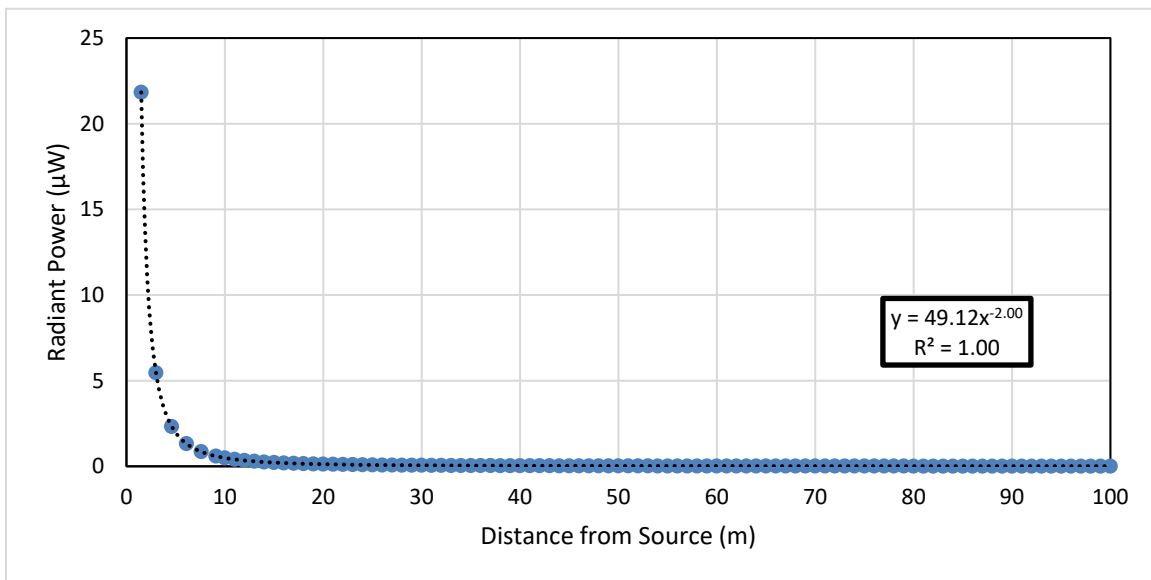


Figure 32. Radiant power plotted over a range of distances from the source (muffler with no attachments) with trend line shown as a black dotted line, and trend line equation and associated root mean squared value given

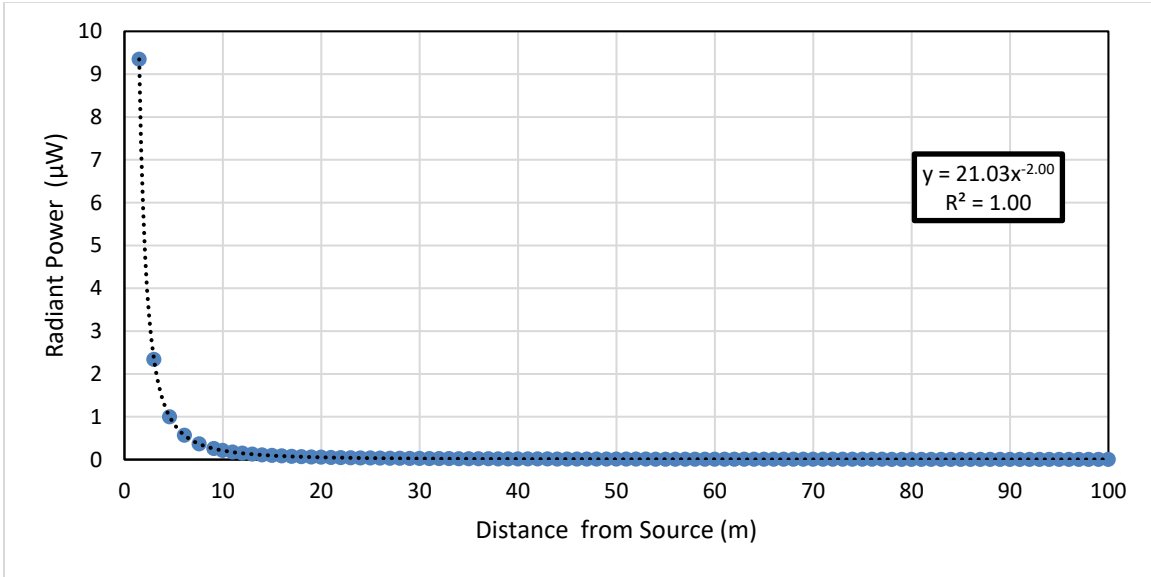


Figure 33. Radiant power plotted over a range of distances from the source (muffler with TEG assembly attached, but no water flowing through cooler) with trend line shown as a black dotted line, and trend line equation and associated root mean squared value given

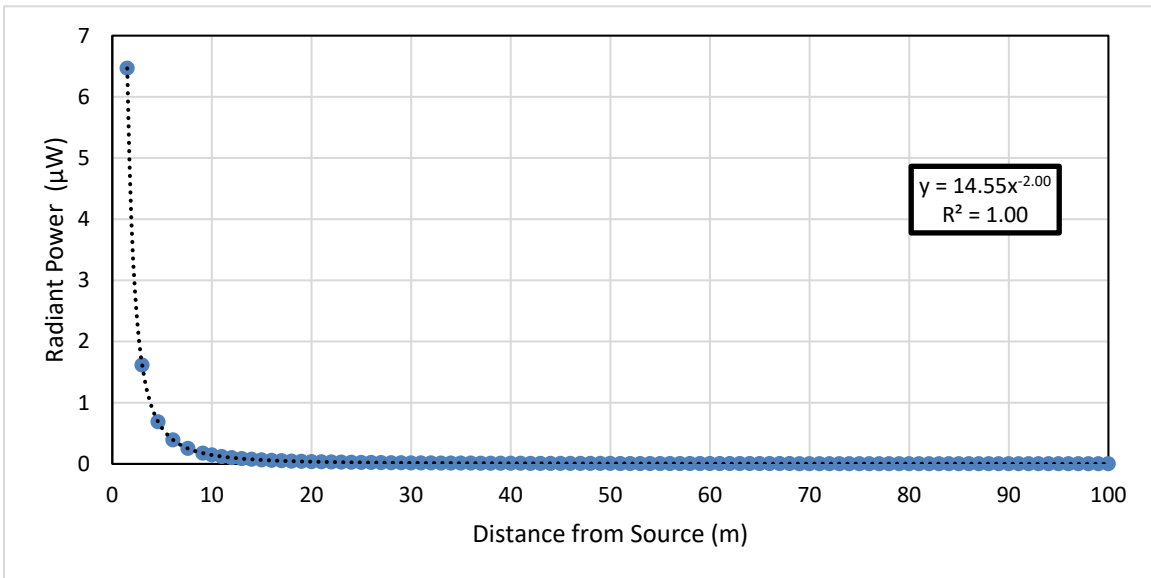


Figure 34. Radiant power plotted over a range of distances from the source (muffler with TEG assembly attached and water flowing through cooler) with trend line shown as a black dotted line, and trend line equation and associated root mean squared value given

3. Predicting Maximum Detection Ranges

To know how far away an IR detector can “see” the generator’s muffler from the surrounding environment, we have to determine the detector’s noise-equivalent power (NEP). The NEP is the radiant flux that gives a signal-to-noise ratio (SNR) of 1 [26]. The noise-equivalent temperature difference (NETD) is the temperature resolution of a sensor and it is calculated by,

$$NETD = \frac{4F^2+1}{A_P} \frac{NEP}{\varepsilon I_M} \quad (16)$$

where F is the f-number of the applied optics, A_P is the area of a pixel, ε is emissivity, and I_M contains radiation characteristics of the measuring object [26]. The simplest solution for I_M [26] is given by,

$$I_{M\infty} = 4\sigma T^3 \quad (17)$$

where σ is the Stefan-Boltzmann constant, and T is the temperature of the measuring object. The f-number, F , of a lens [26] is given by,

$$F = \frac{h_l}{2r_l} \quad (18)$$

where h_l is considered to be the focal length of the lens, and r_l here is the radius of the lens.

Rearranging to get an expression for NEP, we have Equation 19.

$$NEP = \frac{4\sigma A_P \varepsilon T^3 NETD}{4\left(\frac{h_l}{2r_l}\right)^2 + 1} \quad (19)$$

So to estimate the NEP for a given IR detector, we need to know the NETD and detector measurements, such as focal length, radius of lens, and detector pitch to find the pixel area. If a f-number is given, the focal length and radius are not needed. Unless the focal plane array (FPA) is cooled, the detector temperature will be room temperature. For an ideal case, emissivity is approximated to be 1.

In my research, the information required to calculate the NEP of an IR detector was not readily available, perhaps proprietary. I began with the FLIR T1030sc camera I had been using to determine its NEP. Measuring by hand, the lens has a diameter of about 6 cm. The detector has a NETD of 20 mK at 30°C, and a focal length of 0.4 m [24]. I created a MATLAB program for this analysis, provided in Appendix B, and calculated the NEP for the FLIR to be 204 fW (2.04×10^{-13} W).

Afterward, I found IR detectors produced by a French company called Lynred. The first is the Scorpio LW integrated Dewar cooler assembly (IDCA), which is a long wavelength IR (LWIR) detector used for long-range tracking and detection of fast-moving targets [28]. The second is the Daphnis-HD MW IDCA, which is a medium wavelength IR (MWIR) detector used for a variety of military applications aboard aircraft, naval vessels, or ground vehicles [29]. Images of both detectors are shown in Figures 35 and 36.



Figure 35. Scorpio LW IDCA. Source: [28].

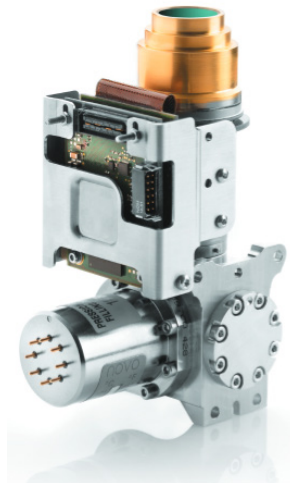


Figure 36. Daphnis-HD MW IDCA. Source: [29].

The Scorpio LW [28] has the following specifications: NETD of 10 mK, FPA operating temperature of 90 K, detector pitch of 15 μm , and a f-number of 2. The Daphnis-HD MW [29] has the following specifications: NETD of 20 mK, FPA operating temperature of 120 K, detector pitch of 10 μm , and a f-number of 2. Again performing the calculations in MATLAB, the NEP for the Scorpio LW is 21.9 fW and the NEP for the Daphnis-HD MW is 46.1 fW. Both are an order of magnitude more sensitive than the FLIR camera, with the Scorpio LW being the most sensitive.

With the NEPs for three different IR detectors known, and the trend line equations for the sets of data known, I moved to graphically determine how far away each IR detector should be able to perceive the generator's muffler in the different configurations. Using my MATLAB program, I plotted curves using the trend line equations, and lines using the NEP values for the three different IR detectors. I adjusted the axes until the intersections of the NEP lines and power curves could be best seen, as shown in Figure 37.

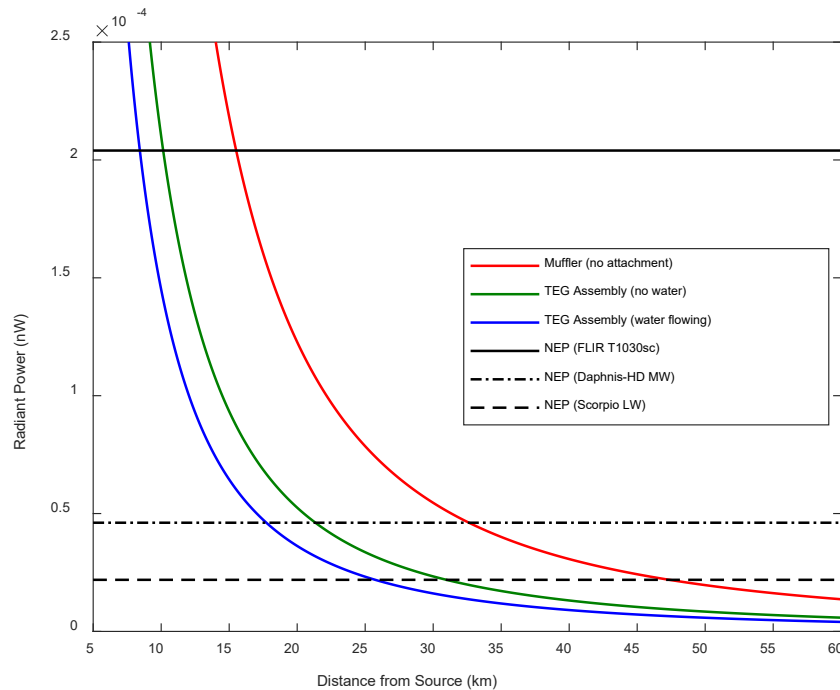


Figure 37. Radiant power vs. distance from source for each configuration of the generator's muffler, along with the NEPs for three different IR detectors

In Figure 37, where the NEP line of a given detector intersects each power versus distance curve is the farthest distance that detector theoretically should be able to still perceive the muffler in its listed configurations, before it blends in with the background noise. The theoretical maximum detection ranges are given in Table 10.

B. RESULTS

Using the trend line equations for radiant power and the graphical analysis from Section A.3. of this chapter, the theoretical maximum distances allowed for each IR detector are given in Table 10. On average, the water-cooled TEG assembly provides a 45.6% reduction in the theoretical maximum detection range, compared to the muffler with nothing attached. There is also a 34.4% reduction when using the TEG assembly and having no water flowing. A significant reason for this drop is a lower emissivity of aluminum (0.46 as shown in the previous section) than that of the muffler (0.86).

Table 10. Theoretical maximum detection ranges for selected IR detectors and the generator's muffler in various configurations

Configuration	Theoretical Maximum Detection Range (km)		
	<i>FLIR T1030sc</i>	<i>Daphnis-HD MW</i>	<i>Scorpio LW</i>
Muffler with no attachment	15.4	32.5	47.5
TEG assembly without water flowing	10.2	21.3	30.9
TEG assembly with water flowing ^a	8.41	17.7	25.7

^aPerformance of water-cooled assembly expected to be improved with a properly working water chiller

As discovered in Chapter II, it is suspected that the water chiller used for the water cooler did not operate under optimal conditions, as it required a refrigerant charge, since the water temperatures were not near the lower values recorded in the past [15]. The experiments for Chapters II and III were conducted concurrently, so the issue was not ascertained until the data was compared after the fact. It is believed that if the water chiller

was operating as designed, the results for the water-cooled variant would be even better than currently assessed.

THIS PAGE INTENTIONALLY LEFT BLANK

IV. DEVELOPMENT AND FABRICATION OF AIR-COOLED RADIATOR ATTACHMENT FOR THERMOELECTRIC WASTE HEAT HARVESTING PROTOTYPE

The purpose of this chapter is to assess how effective a passive cooler would be for the prototype design, both in terms of power generated and IR signature reduction. While water-cooled versions of a TEG waste heat harvester is certainly feasible for ships and other aquatic vehicles, which have access to great amounts of cooling water, it is not practical for expeditionary vehicles on land. It is therefore our goal to, using our existing prototype, design and develop a passive cooler, and then assess its effectiveness.

A. DESIGNING AND FABRICATING THE PASSIVE COOLER

When it comes to combined conduction-convection heat transfer effects [19], an extended surface is used to enhance the heat transfer from the solid to a surrounding fluid or gas. Since the heat transfer rate is directly proportional to the surface area, increasing the surface area increases the rate of heat transfer. One common application is to use fins for cooling objects.

Using SolidWorks software, I generated a thin block of 1.5 cm thickness, with holes to accommodate the bolts needed to fasten it over top of the TEG modules and onto the base plate. Next, I added fins on top with a thickness of 5 mm. Due to material supply constraints for aluminum, the fin height was made 0.91 in. (2.31 cm). The final design is shown in Figure 38.

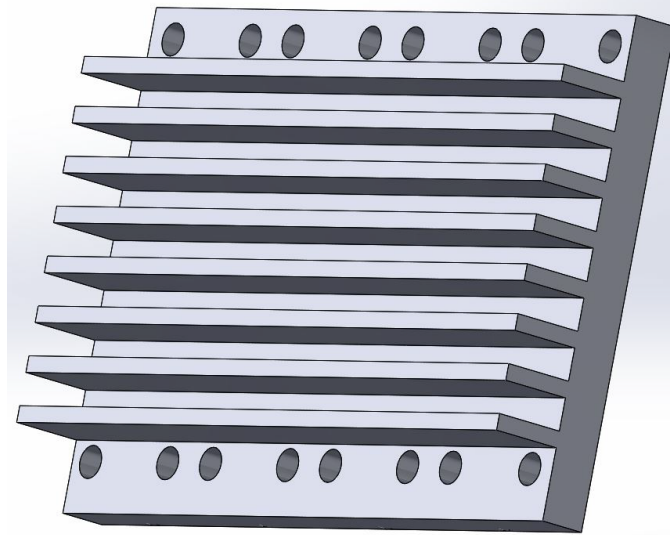


Figure 38. Final design of the passive cooler in SolidWorks

Due to complications due to the COVID-19 pandemic, as well as campus access restrictions, the finished radiator had some deviations from the design. An aluminum block that had been cut in a previous project was all that was available, so the radiator came out 0.3 cm shorter than designed. Technical difficulties also resulted in the bolt holes not being initially drilled in the proper alignment. The fabricated radiator is shown in Figure 39.

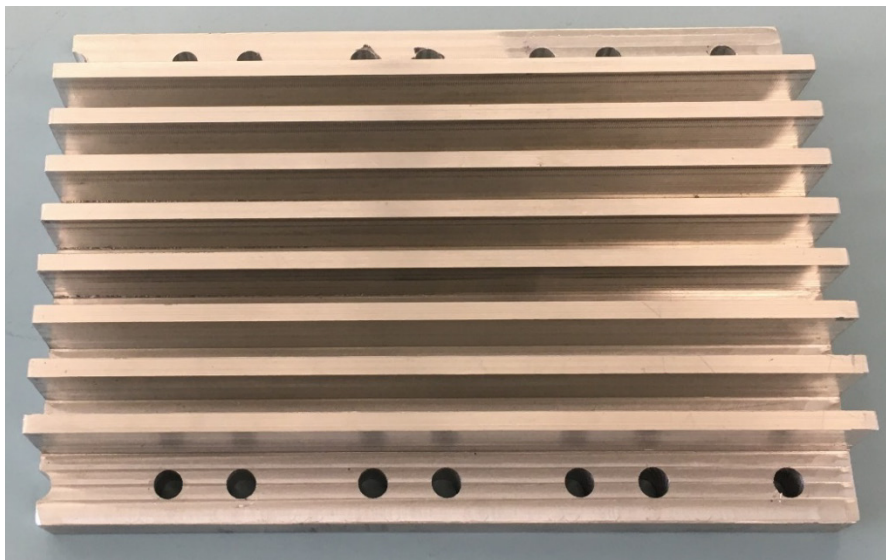


Figure 39. Fabricated radiator

Regardless, the radiator was able to be secured on the base plate and hold the TEG modules as desired, shown in Figure 40. Figure 41 displays the prototype attached to the generator's muffler. The next steps involve assessing how well the radiator might reduce radiant power emitted by the muffler and modeling the prototype in COMSOL. Small portions of the two leftmost TEG modules were slightly exposed and not covered by the radiator.

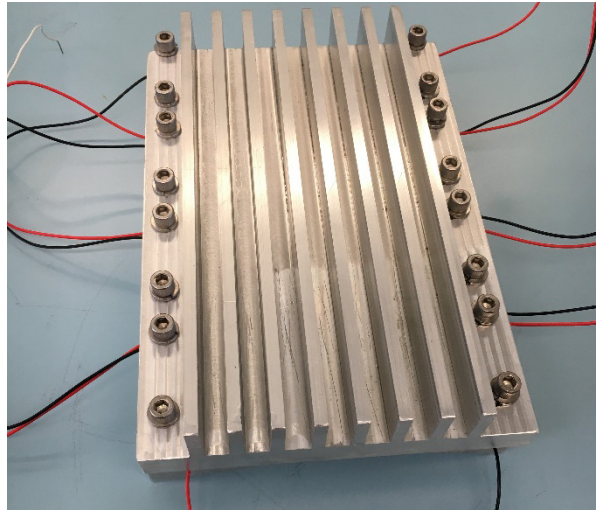


Figure 40. Radiator affixed to base plate, enclosing the TEG modules

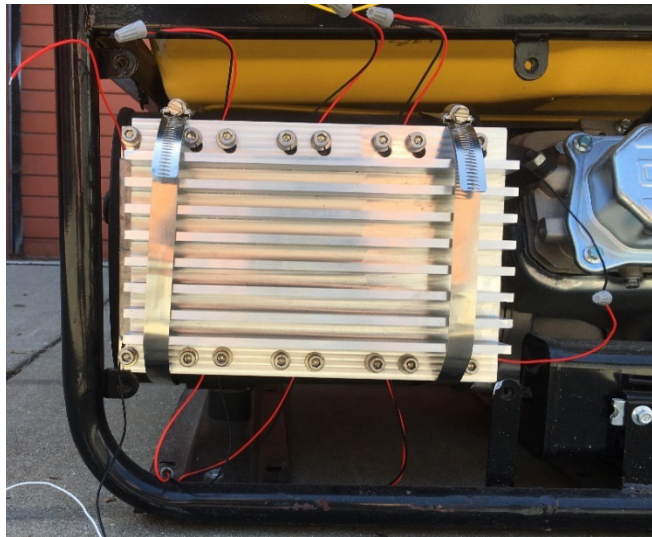


Figure 41. Air-cooled thermoelectric waste heat harvesting prototype

B. ASSESSING THE THERMAL RADIANCE REDUCTION OF THE AIR-COOLED HEAT SINK

The first step was to estimate the emissivity of the radiator. After starting the generator and allowing it 20 minutes to thoroughly warm up, I used a thermocouple to measure the surface temperature of a spot at about 113°C. As in Section A.1. of Chapter III, I had the FLIR camera connected to a laptop running the ResearchIR software. With a ROI at the measured spot, I manually adjusted the inputs for the camera’s distance and emissivity. Through an iterative process, I changed the emissivity value until the temporal plot of the temperature reached around the measured temperature. The emissivity is estimated to be 0.26. The emissivity of the radiator being less than the water cooler seems to make sense, since the surface of the radiator was shinier (more reflective) than that of the water cooler, and the emissivity is directly proportional to the absorbtivity [19].

Using the FLIR camera by itself, I proceeded to take thermal images over varying distances. Starting at 5 ft. from the generator, I took an image of the muffler region at 5-ft. intervals out to 50 ft. The mean radiance is recorded in Table 11.

Table 11. Mean radiance of the radiator

Distance from Source (ft.)	Mean Radiance [W/(sr•cm²)]
5	249.03
10	262.93
15	261.24
20	268.57
25	261.06
30	261.43
35	275.28
40	268.44
45	272.15
50	268.95

Afterward, with the thermal images and the emissivity value, I used the ResearchIR software to analyze the images and record the radiance at each distance. Repeating the process detailed in Section A.2. of Chapter III, I calculated the radiant power emitted and

plotted the data in Figure 42. Using the trend line feature of Microsoft Excel, I developed an equation to use in MATLAB.

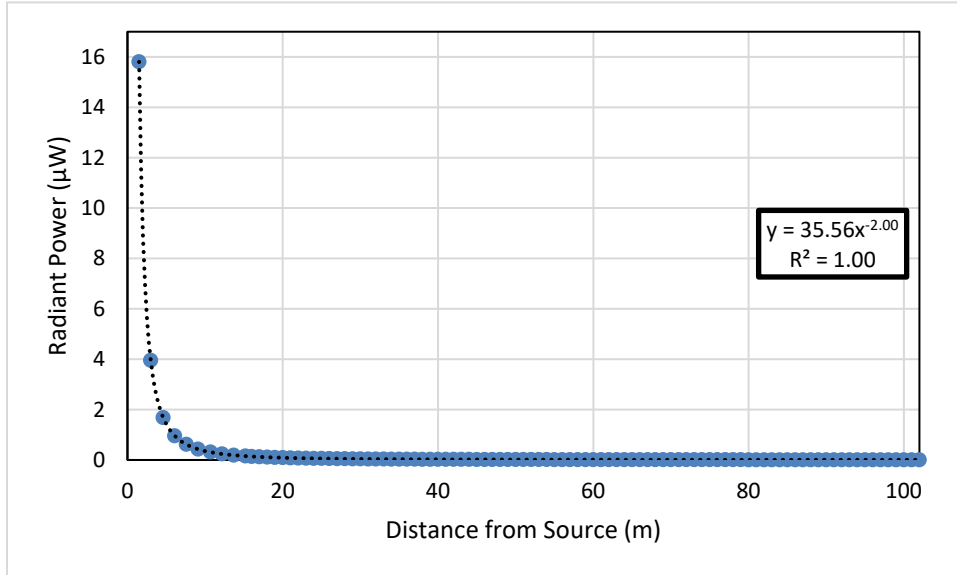


Figure 42. Radiant power plotted over a range of distances from the source (muffler with air-cooled radiator) with trend line shown as a black dotted line, and trend line equation and associated root mean squared value given

Using a MATLAB script, given in Appendix B, I plotted the radiant power curves for the air-cooled prototype, along with the curves for the bare muffler and the water-cooled prototype, with the NEP lines of the IR detectors from Chapter III. The radiant power curves are plotted for four configurations of the muffler in Figure 43.

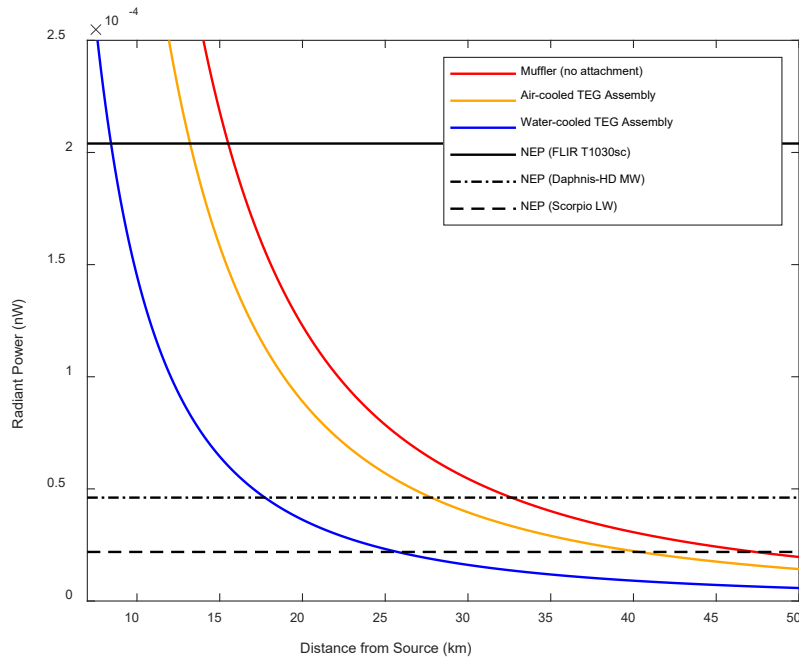


Figure 43. Radiant power vs. distance from the source for each configuration of the generator’s muffler, along with the NEPs for three different IR detectors

As before, where the NEP lines intersect the radiant power curves are the theoretical maximum detection ranges for each IR detector to perceive the muffler in its different configurations. These ranges are tabulated in Table 12. From Chapter III, the theoretical maximum detection range reduction for the water-cooled prototype is 45.6%. The air-cooled prototype does not perform as well, with an average reduction of 14.7%. The air-cooled prototype actually performs worse than the water-cooled assembly without water, perhaps due to the empty cavity inside of the water cooler acting as an insulator. It is important to note that if the water chiller was working properly, the reduction of the emitted power by the water-cooled block would have been greater than 45%. Still, the air-cooled prototype would require an aircraft with a high-end camera to get 10 extra km to see the generator.

Table 12. Theoretical maximum detection ranges for selected IR detectors and the generator’s muffler in various configurations

Configuration	Theoretical Maximum Detection Range (km)		
	<i>FLIR T1030sc</i>	<i>Daphnis-HD MW</i>	<i>Scorpio LW</i>
Muffler with no attachment	15.4	32.5	47.5
Water-cooled prototype ^a	8.41	17.7	25.7
Air-cooled prototype	13.2	27.7	40.3

^aPerformance of water-cooled assembly expected to be improved with a properly working water chiller

C. COMSOL MODEL OF AIR-COOLED THERMOELECTRIC WASTE-HEAT HARVESTING PROTOTYPE

The last step in the performance assessment of the air-cooled assembly is to build a model of the air-cooled prototype in COMSOL and assess its theoretical performance. The COMSOL models for the muffler, base plate, and TEG modules remain unchanged from Chapter II. The radiator was recreated in COMSOL and is shown in Figure 44. The original plan was to include grooves for thermocouples in future experiments, however they were left out when the radiator was built. As such, the underside of the COMSOL radiator model is flat as well.

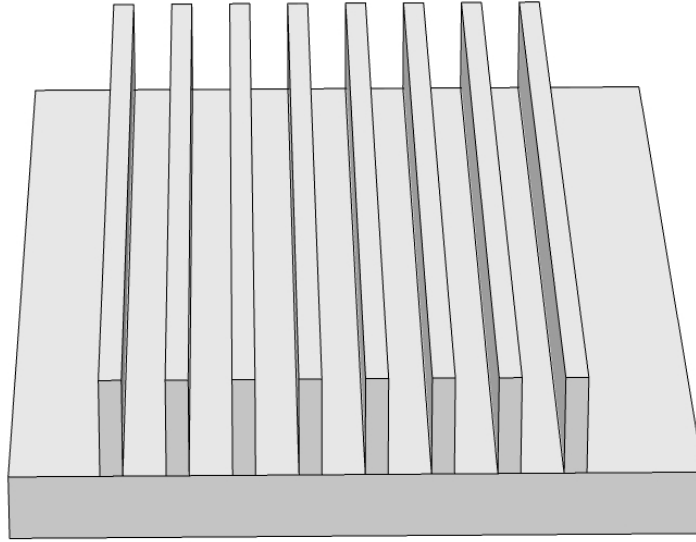


Figure 44. COMSOL model of radiator

As mentioned earlier, the radiator came out shorter than originally planned, and with the problem with bolt hole alignment, the radiator sat slightly offset to one side when bolted into place. As such, part of two TEG modules are left exposed, as shown in Figure 45. Since the goal is to recreate what was observed experimentally, this imperfection was carried on into the COMSOL model, seen in Figure 46.

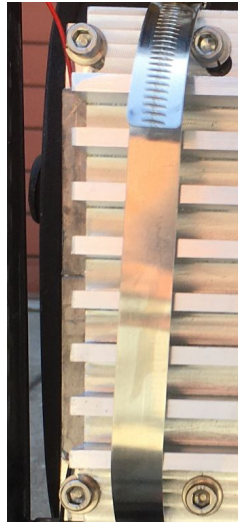


Figure 45. Exposed TEG modules due to shortened radiator length and misalignment of bolts

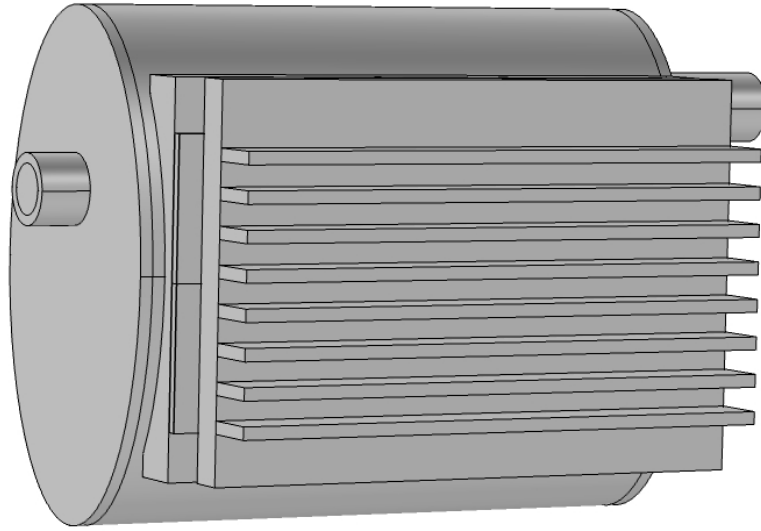


Figure 46. COMSOL model of air-cooled prototype

To set up the model, the convective heat transfer coefficient and the emissivity are needed to account for convective and radiative heat losses by the cooler element. Since the fins run horizontally, approximating free convection on a flat, vertical plate will not suffice. However, if examining one fin, it can be approximated as a flat plate in parallel flow. The average Nusselt number becomes,

$$\overline{Nu} = 0.664Re^{1/2}Pr^{1/3} \quad Pr \gtrsim 0.6 \quad (20)$$

where Pr is the Prandtl number, and Re is the Reynolds number [19]. The Reynolds number is given by,

$$Re = \frac{VL}{\nu} \quad (21)$$

where V is the velocity of the airflow, L is the length of the plate, and ν is the kinematic viscosity [19]. The air velocity can be assumed to be that of a light breeze, about 3 m/s. The parameters for air, such as the kinematic viscosity, ν , the thermal conductivity, k (used in Equation 3 in Chapter II), and the Prandtl number, Pr , must be assessed at the film temperature [19], which is given in Equation 8 in Chapter II. The film temperature requires both the surface temperature and the ambient temperature. The air temperature at the time of the experiment was about 68°F (20°C). Once the parameters are found in a table for that

film temperature, the Reynolds number can be calculated in Equation 21, and then the average Nusselt number in Equation 20. Using Equation 3 in Chapter II, the average convective heat transfer coefficient can be determined. A MATLAB script was written to aid in the repeatability of this experiment and is provided in Appendix A.

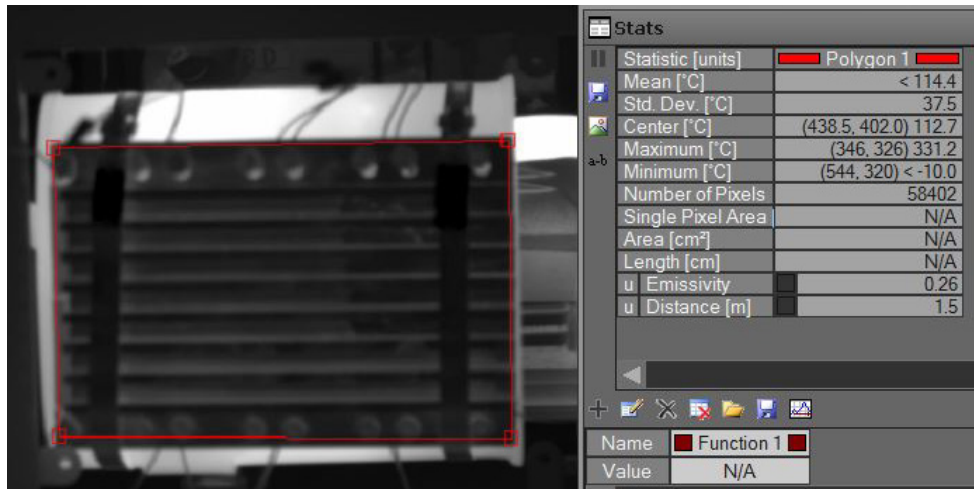


Figure 47. FLIR image of the radiator in ResearchIR, with data given on the mean surface temperature within the region of interest (ROI), shown as a red box

By means of the ResearchIR software and a FLIR image taken, seen in Figure 45 above, the mean surface temperature is about 114.4°C. Using this value for the mean surface temperature along with the aforementioned process to find the convective heat transfer coefficient, an initial h value was calculated as 14.51 W/(m²•K). From earlier, the emissivity is 0.26.

Running the simulation once, I obtained an average surface temperature of 192.4°C on the radiator, which is certainly above what was observed. The only variable to be able to change in the model is the convective heat transfer coefficient. After all, the steps taken to reach the value above were only an approximation. After multiple simulations, the final value for h was 49 W/(m²•K) to achieve an average surface temperature of the facing surfaces of 114.8°C. With my approach to determine h , the air velocity needed to reach that value is about 35 m/s (68 knots). While there was a light breeze the day of the

experiment, it certainly was not that strong. So using Equation 20 to find the Nusselt number is not the proper method to use. Still, it served as a decent starting point.

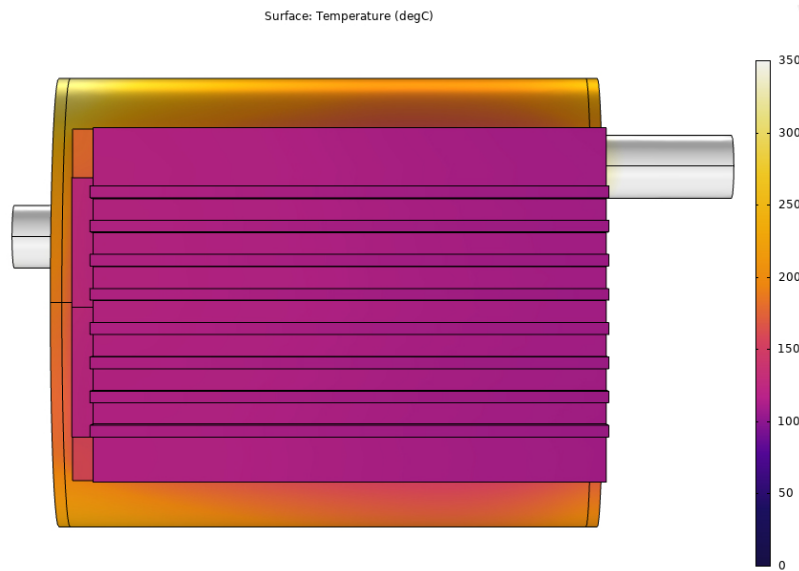


Figure 48. Temperature profile from heat transfer simulation for the air-cooled prototype model in COMSOL

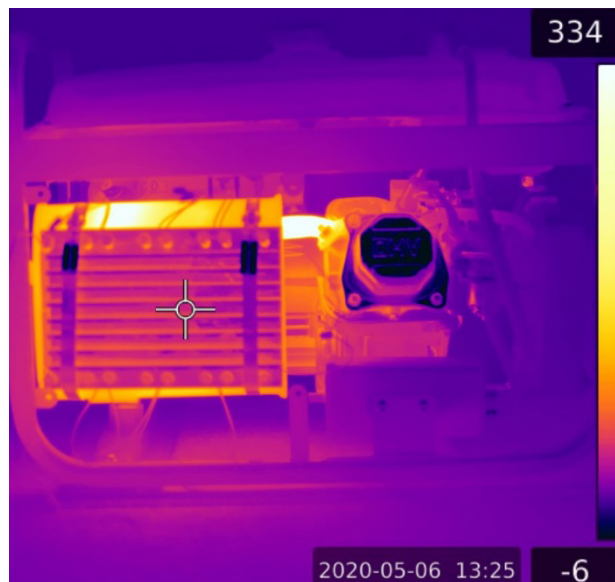


Figure 49. FLIR image of the generator with the air-cooled prototype attached

The temperature profile from the heat transfer simulation is shown in Figure 48, with a comparison to the FLIR thermal image in Figure 49. From the model, the maximum temperature of the hot side of each TEG module was recorded, as well as the minimum temperature of the cool side of TEG module. These values, along with the differential temperature of the cool side of TEG module. These values, along with the differential temperature, are given in Table 13.

Table 13. Temperature measurements on TEG modules derived from COSMOL model

TEG Module	T_{hot} (°C)	T_{cool} (°C)	ΔT (°C)
1	175.46	121.08	54.38
2	159.10	117.63	41.47
3	148.03	115.01	33.02
4	148.66	112.95	35.71
5	162.44	119.43	43.01
6	149.38	116.56	32.82
7	141.76	114.25	27.51
8	141.95	112.28	29.67

To compare the results to something, the adjusted water-cooled model from Section B.2. of Chapter II was selected. As shown graphically in Figure 50, using an air-cooled heat sink generates lower differential temperatures in the COMSOL model than using a water-cooled heat sink. Still, the differential temperatures generated by the air-cooled heat sink are substantial.

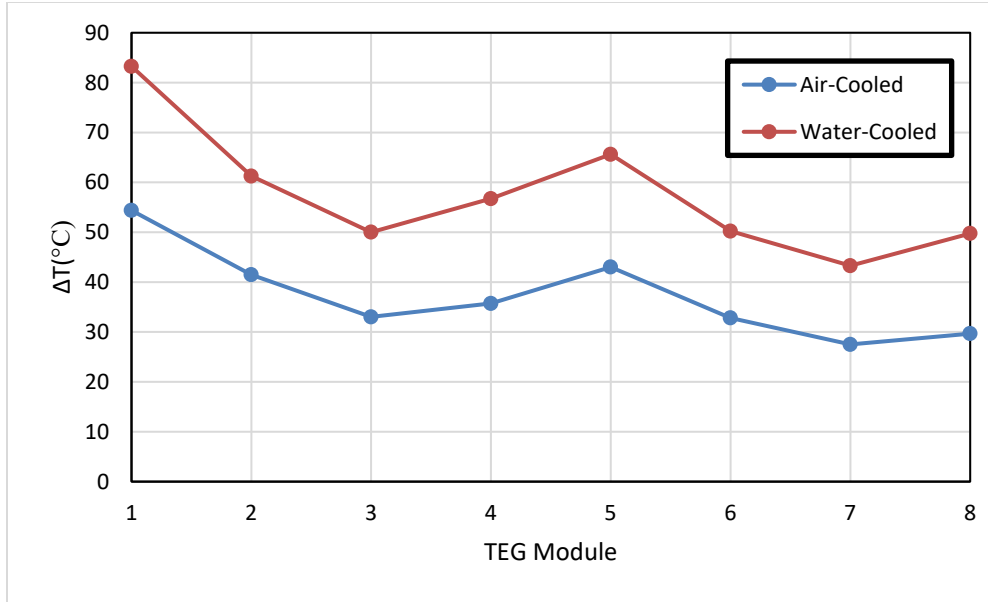


Figure 50. Differential temperatures from COMSOL simulations using both water-cooled and air-cooled heat sink designs

With the differential temperatures recorded, it is time to determine the theoretical electrical power performance. The same procedures from Chapter II Section B are used again here, with the same load resistance values. Since the open-circuit voltages generated by the TEG modules are dependent on the differential temperature values, we can expect the air-cooled model to exhibit poorer performance than the water-cooled model. Table 14 gives the theoretical values for voltage, current, and power for the air-cooled model. Figures 51, 52, and 53 display this information graphically, with comparisons to the water-cooled model shown.

Table 14. Theoretical voltage, current, and power values across load resistances, derived from TEG module open-circuit voltage and internal resistance equations, as a function of differential temperatures obtained from COSMOL model using an air-cooled heat sink

$R_{load} (\Omega)$	$V_{load} (V)$	$I_{load} (A)$	Power (W)
1.00	0.266	0.266	0.071
10.00	1.855	0.185	0.344
20.00	2.777	0.139	0.386
33.00	3.454	0.105	0.361
47.00	3.888	0.083	0.322
55.00	4.063	0.074	0.300

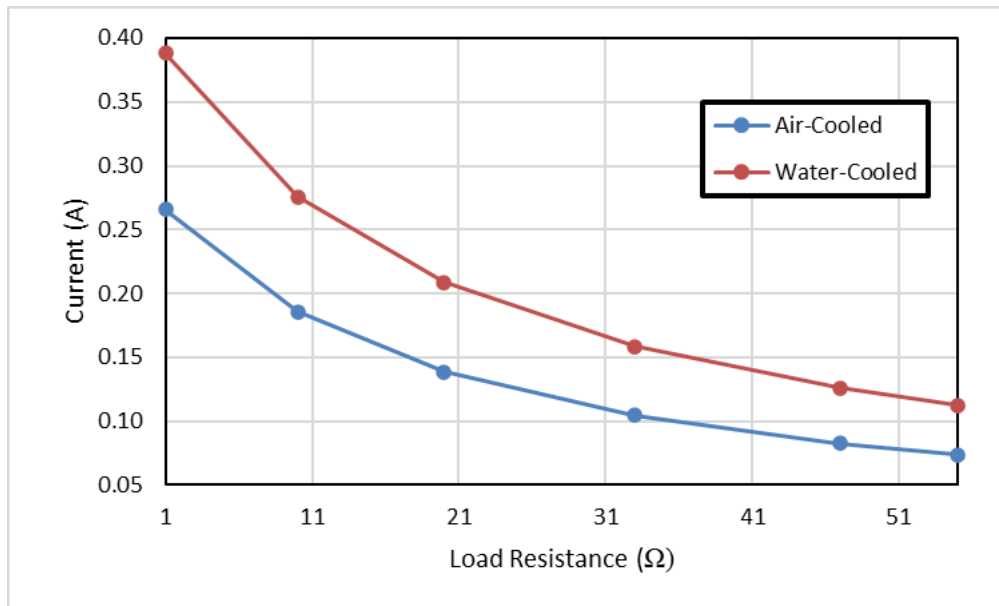


Figure 51. Theoretical current vs. load resistances for COMSOL models using water-cooled and air-cooled heat sinks

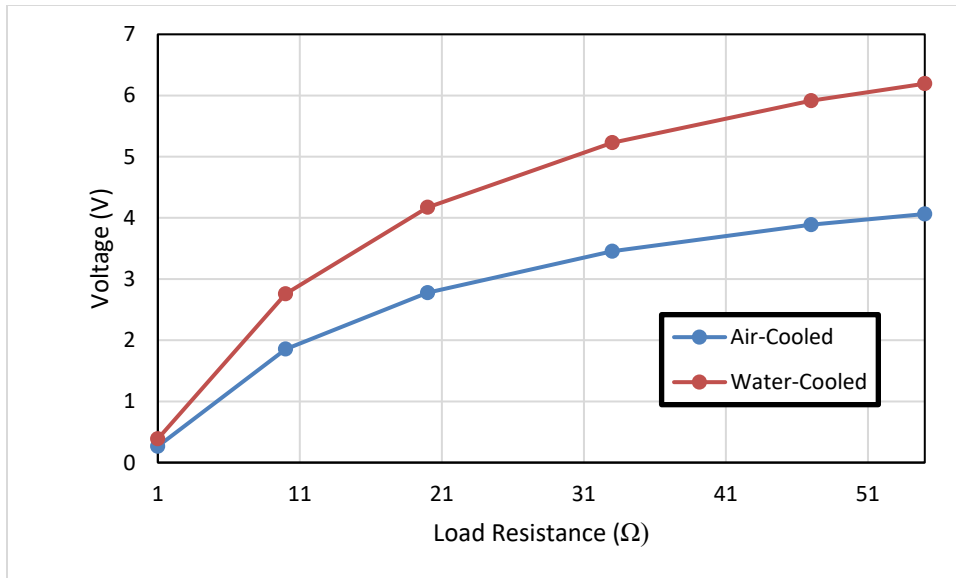


Figure 52. Theoretical voltage vs. load resistances for COMSOL models using water-cooled and air-cooled heat sinks

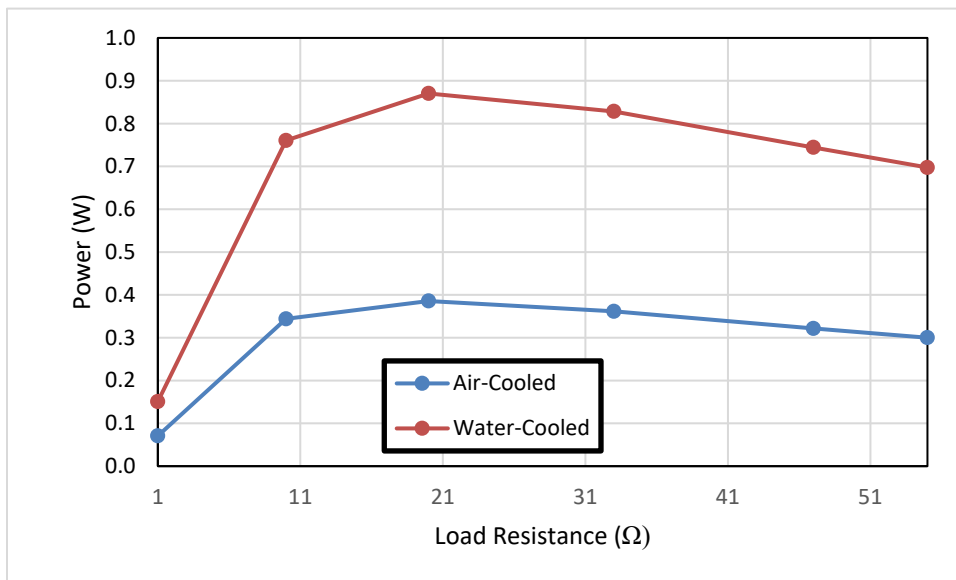


Figure 53. Theoretical power vs. load resistances for COMSOL models using water-cooled and air-cooled heat sinks

During the experiment, the open-circuit voltage was measured by way of a multimeter at 8.83 V after 20 minutes of operation. If the open-circuit voltages from the model are summed it, the theoretical open-circuit voltage is 5.52 V, which is a difference

of 37.5% below the experimental measurement. This may not be a perfect comparison, but serves to show that the model is close to the real thing.

From the analysis, the power generated by the air-cooled model lags well behind that of the water-cooled model. The peak power value, seen at 20 Ω , is 55.6% below the peak power of the water-cooled model. However, this shows that some waste heat energy can still be recovered by using the air-cooled heat sink. More work could be performed in the future to optimize the design in order to maximize its performance. A comprehensive list of parameters entered into the COMSOL model is provided in Appendix C.

V. CONCLUSION

A. ANALYSIS OF RESULTS

In Chapter II, it was shown that the conditions for the water-cooled waste heat harvesting prototype can be modeled in COMSOL. The differential temperatures for both the simulation and the experimental data were close to each other, albeit mirrored. The main source of discrepancy is the model oversimplification of the inner workings of the muffler. TEG module placement is shown not to matter for this model. While the COMSOL model produces lower performance, in terms of power, than what was obtained experimentally, a useful theoretical approximation can be had for load resistances of less than 10Ω .

In Chapter III, having the water-cooled prototype attached to the muffler was shown to reduce the maximum range of detection by IR sensors by 45.6% on average, when compared to having nothing attached to the muffler. After the experiment was conducted, it was discovered the water chiller used had degraded performance due to the need for its refrigerant to be recharged. As such, it is believed the maximum detection range could be reduced ever further if used with a properly functioning water chiller.

In Chapter IV, a passive, air-cooled radiator attachment was designed and built. While electrical load testing has yet to be accomplished, the COMSOL model showed some promise. The peak power generated by this air-cooled model lagged behind the water-cooled model by 55.6%. While the ability of the air-cooled prototype to reduce the thermal signature was not as good as that of the water-cooled prototype, its 14.7% reduction of the maximum range of detection by IR sensors is still useful. If the design could be enhanced, it would be beneficial in not needing additional equipment, like a water chiller or water pump. Not having this extra equipment would help reduce the impact of parasitic losses to the vehicle. Once the thermal model is validated, it can be used to further optimize the cooler design and improve the power output of the system.

B. PROPOSED FUTURE WORK

First, further testing of the air-cooled prototype would involve experimentally measuring current and voltage over varying load resistances. Such testing would validate the findings derived from the COMSOL model. The process for the air-cooled prototype could be repeated for a radiator that has an improved fit onto the base plate.

Second, both the water-cooled and air-cooled COMSOL models could be enhanced to calculate the voltage, current, and power directly from the temperature differences of each TEG module, derived from the model's simulation results. These could be coupled with the electric circuit feature of COMSOL into an enhanced multi-physics model to obtain the total power output within the model. With a properly functioning water chiller, the inputs can be adjusted to match the new observed conditions. Additionally, more experiments can be done on the water-cooled prototype with more load resistances in order to further validate the COMSOL model's performance. Also, acquiring a replacement muffler to cut open would aid in making the muffler model more true to form in COMSOL.

Third, the thermal images of the generator in its various configurations can be retaken over greater distances. This might allow a more reliable analysis of how its radiant power changes over increased distances. If a drone with an IR detector can be acquired, then more tests could be performed to determine how the visibility of the muffler can be reduced.

Fourth, efforts could be made to optimize both the water-cooled and air-cooled designs. For the air-cooled heat sink, different heat exchanger designs could be explored, such as adding more fins, or trying other geometries. Novel designs could be explored as well, such as hollow, segmented tubes [30].

Ultimately, the goal of this research is to one day improve the energy efficiency in the fleet. Water-cooled thermoelectric waste heat harvesters could prove viable solutions to ships and auxiliary boats. While water-cooled variants could still be viable for expeditionary vehicles in the field, air-cooled variants may prove just as good or better, and without the added weight of pumps and reservoirs of cooling liquids.

APPENDIX A. MATLAB CODE FOR CALCULATING CONVECTIVE HEAT TRANSFER COEFFICIENTS

A. H VALUE FOR MUFFLER

```
clear all
close all
clc

g = 9.81;           % gravitational acceleration (m/s^2)
L = 0.2032;        % height of the muffler/characteristic length (m)
Ts = 279 + 273;    % muffler's mean surface temperature (K)
Tinf = 16 + 273;   % approximate ambient air temperature (K)
% note: ambient air temperature corresponds to typical Monterey weather of
% 60 degF

Tf = (Ts + Tinf)/2; % film temperature (K)
fprintf('Film Temperature (K): %g\n',Tf)
beta = 1/Tf;       % expansion coefficient (1/K)

% Tf = 420.5 K, and table has values 400 K and then 450 K, so I developed
% best-fit equations for k, nu, and Pr from Appendix A.4 of Incropera et
% al., for air between 100 and 800 K.

k = -3e-8*Tf^2 + 1e-4*Tf - 0.0002; % approx. thermal conductivity for air (W/m*K)
nu = 6e-10*Tf^1.7869;              % approx. kinematic viscosity for air (m^2/s)
Pr = 4e-13*Tf^4 - 1e-9*Tf^3 + 1e-6*Tf^2 - 8e-4*Tf + 0.8557; % approx. Prandtl number for
air

Gr = (g*beta*(Ts - Tinf)*L^3)/(nu^2); % Grashof number
Ra = Gr*Pr;                          % Rayleigh number

if Ra<= 1e9
    Nu = 0.68 + (0.67*Ra^(1/4))/(1 + (0.492/Pr)^(9/16))^(4/9); % Nusselt number for a
flat plate approximation
else
    disp('Not Laminar Flow')
    disp('Different approach needed')
end

h = (Nu*k)/L; % convective heat transfer coefficient (W/m^2*K)
fprintf('Convective Heat Transfer Coefficient, h (W/m^2*K): %g\n',h)
```

Film Temperature (K): 420.5

Convective Heat Transfer Coefficient, h (W/m²*K): 7.29506

B. H VALUE FOR WATER COOLER

```
clear all
close all
clc

g = 9.81;           % gravitational acceleration (m/s^2)
L = 0.152;         % height of the water cooler/characteristic length (m)
Ts = 43.6 + 273;   % cooler's mean surface temperature (K)
Tinf = 16 + 273;   % approximate ambient air temperature (K)
% note: ambient air temperature corresponds to typical Monterey weather of
% 60 degF

Tf = (Ts + Tinf)/2; % film temperature (K)
fprintf('Film Temperature (K): %g\n',Tf)
beta = 1/Tf;       % expansion coefficient (1/K)

% values from Appendix A.4 of Incropera et al. for air at atmospheric
% pressure
% Tf = 302.8 K, so taking the values for 300 K
Pr = 0.707;        % Prandtl number for air
nu = 15.89e-6;     % kinematic viscosity for air (m^2/s)
k = 26.3e-3;       % thermal conductivity for air (W/m*K)

Gr = (g*beta*(Ts - Tinf)*L^3)/(nu^2); % Grashof number
Ra = Gr*Pr;        % Rayleigh number

if Ra <= 1e9
    Nu = 0.68 + (0.67*Ra^(1/4))/(1 + (0.492/Pr)^(9/16))^(4/9); % Nusselt number for a
    flat plate approximation
else
    disp('Not Laminar Flow')
    disp('Different approach needed')
end

h = (Nu*k)/L;      % convective heat transfer coefficient (W/m^2*K)
fprintf('Convective Heat Transfer Coefficient, h (W/m^2*K): %g\n',h)
```

Film Temperature (K): 302.8

Convective Heat Transfer Coefficient, h (W/m²*K): 4.96058

C. H VALUE FOR PASSIVE RADIATOR

```
clear all
close all
clc

L = 0.22;          % fin width (m)
Ts = 114 + 273;   % radiator's mean surface temperature (K)
```

```

Tinf = 20 + 273;    % approximate ambient air temperature (K)
V = 3;             % assumed air flow velocity (m/s)
% V = 35;         % air velocity needed to reach a h value of 49 W/m^2*K (m/s)
% note: ambient air temperature corresponds to weather report for Monterey of 68 degF

Tf = (Ts + Tinf)/2; % film temperature (K)
fprintf('Film Temperature (K): %g\n',Tf)
beta = 1/Tf;       % expansion coefficient (1/K)

% For first iteration: Tf = 340 K, and table has values 300 K and then 350 K, so I
developed
% best-fit equations for k, nu, and Pr from Appendix A.4 of Incropera et
% al., for air between 100 and 800 K.
k = -3e-8*Tf^2 + 1e-4*Tf - 0.0002; % approx. thermal conductivity for air (W/m*K)
nu = 6e-10*Tf^1.7869;             % approx. kinematic viscosity for air (m^2/s)
Pr = 4e-13*Tf^4 - 1e-9*Tf^3 + 1e-6*Tf^2 - 8e-4*Tf + 0.8557; % approx. Prandtl number for
air

Re = (V*L)/nu;                   % Reynolds number
Nu = 0.664*Re^(1/2)*Pr^(1/3);    % Nusselt number

h = (Nu*k)/L;                   % convective heat transfer coefficient (W/m^2*K)
fprintf('Convective Heat Transfer Coefficient, h (W/m^2*K): %g\n',h)

```

Film Temperature (K): 340

Convective Heat Transfer Coefficient, h (W/m²*K): 14.508

[Published with MATLAB® R2018b](#)

THIS PAGE INTENTIONALLY LEFT BLANK

APPENDIX B. MATLAB CODE FOR NEP CALCULATIONS AND RADIANT POWER PLOT

A. INITIAL TEST

```
clear all
close all
clc

sigma = 5.6704e-8; % Stefan-Boltzmann constant (W/M^2*K^4)

% trendline equations from data
x = linspace(1, 100000, 1000);
Pm = 4.91e-5*x.^-2.*1e9; % radiant power for muffler only (nW)
Ptn = 2.1e-5*x.^-2.*1e9; % radiant power for TEG assembly, no water flowing (nW)
Ptw = 1.45e-5*x.^-2.*1e9; % radiant power for TEG assembly, water flowing (nW)

% calculating noise equivalent power (NEP)
epsilon = 1; % assumed emissivity

% FLIR T1030sc
NETD1 = 20e-3; % noise equivalent temperature difference (NETD) (K)
T1 = 30 + 273; % operating temperature (K)
lambda1 = 17e-6; % detector pitch (m)
d_lens1 = 0.06; % diameter of sensor lens for FLIR T1030sc (m)
A_pix1 = (lambda1)^2; % pixel area (m^2)
h1 = 0.4; % focal distance (m)
F1 = h1/d_lens1; % f-number
NEP1 = ((NETD1.*epsilon.*4.*sigma.*A_pix1.*T1^3)./(4.*(F1.^2) + 1)); % NEP (W)
fprintf('NEP for FLIR T1030sc (fW): %g\n', NEP1*1e15)

% Daphnis-HD MW
NETD2 = 20e-3; % NETD (K)
T2 = 120; % FPA operating temperature (K)
F2 = 2; % f-number
lambda2 = 10e-6; % detector pitch (m)
A_pix2 = lambda2^2; % pixel area (m^2)
NEP2 = ((NETD2.*epsilon.*4.*sigma.*A_pix2.*T2^3)./(4.*(F2.^2) + 1)); % NEP (W)
fprintf('NEP for Daphnis-HD MW (fW): %g\n', NEP2*1e15)

% Scorpio LW
NETD3 = 10e-3; % NETD (K)
T3 = 90; % FPA operating temperature (K)
F3 = 2; % f-number
lambda3 = 15e-6; % detector pitch (m)
A_pix3 = lambda3^2; % pixel area (m^2)
NEP3 = ((NETD3.*epsilon.*4.*sigma.*A_pix3.*T3^3)./(4.*(F3.^2) + 1)); % NEP (W)
fprintf('NEP for Scorpio LW (fW): %g\n', NEP3*1e15)
```

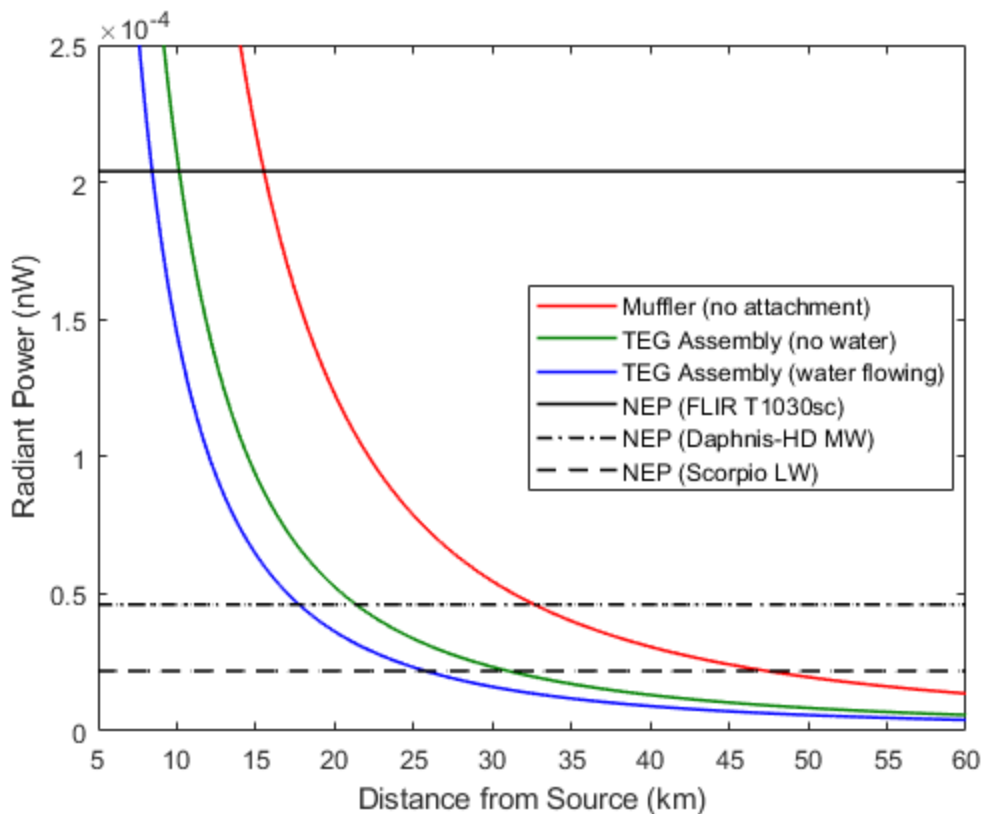
```

% create arrays to plot
Pmi na = 1e9*NEP1*ones(1,length(x)); % FLIR
Pmi nb = 1e9*NEP2*ones(1,length(x)); % Daphnis
Pmi nc = 1e9*NEP3*ones(1,length(x)); % Scorpio LW
X = x./1000; % converting to have plot be in km

plot(X,Pm,'r','linewidth',1.1)
hold on
plot(X,Ptn,'color',[0 0.5 0],'linewidth',1.1)
plot(X,Ptw,'b','linewidth',1.1)
plot(X,Pmi na,'k','linewidth',1.1)
plot(X,Pmi nb,'-k','linewidth',1.1)
plot(X,Pmi nc,'-k','linewidth',1.1)
ylim([0 2.5e-4])
xlim([5 60])
xlabel('Distance from Source (km)')
ylabel('Radiant Power (nW)')
legend('Muffler (no attachment)','TEG Assembly (no water)','TEG Assembly (water flowing)','NEP (FLIR T1030sc)','NEP (Daphnis-HD MW)','NEP (Scorpio LW)','location','best')

```

NEP for FLIR T1030sc (fW): 203.993
NEP for Daphnis-HD MW (fW): 46.1104
NEP for Scorpio LW (fW): 21.8844



B. INCLUDING RADIATOR

```
clear all
close all
clc

sigma = 5.6704e-8; % Stefan-Boltzmann constant (W/M^2*K^4)

% trendline equations from data
x = linspace(1, 10000, 1000);
Pm = 4.91e-5*x.^-2.*1e9; % radiant power for muffler only (nW)
Ptw = 1.45e-5*x.^-2.*1e9; % radiant power for water-cooled TEG assembly (nW)
Ptr = 3.56e-5*x.^-2.*1e9; % radiant power for air-cooled TEG assembly (nW)

% calculating noise equivalent power (NEP)
epsilon = 1; % assumed emissivity

% FLIR T1030sc
NETD1 = 20e-3; % noise equivalent temperature difference (NETD) (K)
T1 = 30 + 273; % operating temperature (K)
lambda1 = 17e-6; % detector pitch (m)
d_lens1 = 0.06; % diameter of sensor lens for FLIR T1030sc (m)
A_pix1 = (lambda1)^2; % pixel area (m^2)
h1 = 0.4; % focal distance (m)
F1 = h1/d_lens1; % f-number
NEP1 = ((NETD1.*epsilon.*4.*sigma.*A_pix1.*T1^3)./(4.*(F1.^2) + 1)); % NEP (W)
fprintf('NEP for FLIR T1030sc (fW): %g\n', NEP1*1e15)

% Daphnis-HD MW
NETD2 = 20e-3; % NETD (K)
T2 = 120; % FPA operating temperature (K)
F2 = 2; % f-number
lambda2 = 10e-6; % detector pitch (m)
A_pix2 = lambda2^2; % pixel area (m^2)
NEP2 = ((NETD2.*epsilon.*4.*sigma.*A_pix2.*T2^3)./(4.*(F2.^2) + 1)); % NEP (W)
fprintf('NEP for Daphnis-HD MW (fW): %g\n', NEP2*1e15)

% Scorpio LW
NETD3 = 10e-3; % NETD (K)
T3 = 90; % FPA operating temperature (K)
F3 = 2; % f-number
lambda3 = 15e-6; % detector pitch (m)
A_pix3 = lambda3^2; % pixel area (m^2)
NEP3 = ((NETD3.*epsilon.*4.*sigma.*A_pix3.*T3^3)./(4.*(F3.^2) + 1)); % NEP (W)
fprintf('NEP for Scorpio LW (fW): %g\n', NEP3*1e15)

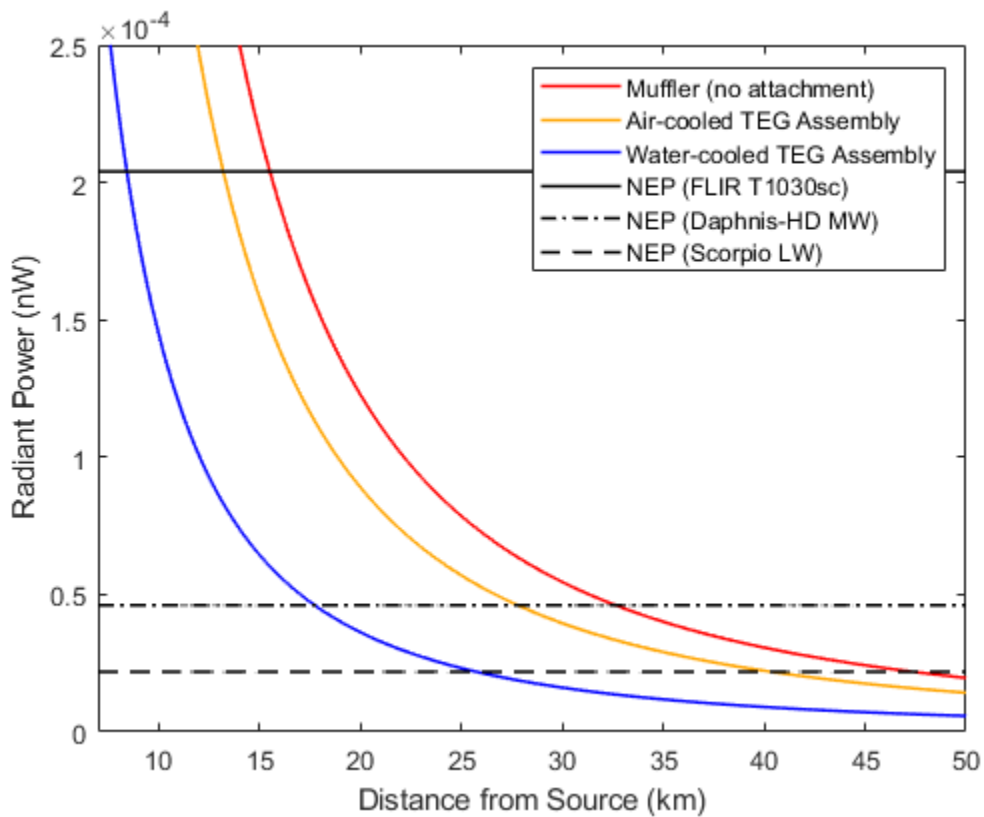
% create arrays to plot
Pmi na = 1e9*NEP1*ones(1, length(x)); % FLIR
Pmi nb = 1e9*NEP2*ones(1, length(x)); % Daphnis
Pmi nc = 1e9*NEP3*ones(1, length(x)); % Scorpio LW
X = x./1000; % converting to plot in km
```

```

plot(X, Pm, 'r', 'linewidth', 1.1)
hold on
plot(X, Ptr, 'color', [1, 0.647, 0], 'linewidth', 1.1)
plot(X, Ptw, 'b', 'linewidth', 1.1)
plot(X, Pmina, 'k', 'linewidth', 1.1)
plot(X, Pminb, '-.k', 'linewidth', 1.1)
plot(X, Pminc, '--k', 'linewidth', 1.1)
ylim([0 2.5e-4])
xlim([7 50])
xlabel('Distance from Source (km)')
ylabel('Radiant Power (nW)')
legend('Muffler (no attachment)', 'Air-cooled TEG Assembly', 'Water-cooled TEG
Assembly', 'NEP (FLIR T1030sc)', 'NEP (Daphnis-HD MW)', 'NEP (Scorpio
LW)', 'location', 'northeast')

```

NEP for FLIR T1030sc (fW): 203.993
NEP for Daphnis-HD MW (fW): 46.1104
NEP for Scorpio LW (fW): 21.8844



Published with MATLAB® R2018b

APPENDIX C. COMSOL INPUT PARAMETERS

A. MATERIALS

Graphite		
Density	2210	kg/m ³
Thermal conductivity	1950	W/(m•K)
Heat capacity at constant pressure	709	J/(kg•K)
Silicon nitride		
Density	2400	kg/m ³
Thermal conductivity	16	W/(m•K)
Heat capacity at constant pressure	691	J/(kg•K)

B. ADJUSTED WATER-COOLED MODEL

Ambient air temperature	16	°C
Muffler		
Inflow temperature	635	°C
Inlet flow rate	7e-3	m ³ /s
Convective heat transfer coefficient	7.295	W/(m ² •K)
Emissivity	0.86	
Upstream pressure	1	atm
Water cooler		
Inflow temperature	12	°C
Inlet flow rate	6.309e-5	m ³ /s
Convective heat transfer coefficient	4.96	W/(m ² •K)
Emissivity	0.46	
Upstream pressure	1	atm

C. AIR-COOLED MODEL

Ambient air temperature	20	°C
Muffler		
Inflow temperature	600	°C
Inlet flow rate	6.24e-3	m ³ /s
Convective heat transfer coefficient	7.295	W/(m ² •K)
Emissivity	0.86	
Upstream pressure	1	atm
Radiator		
Convective heat transfer coefficient	49	W/(m ² •K)
Emissivity	0.26	

LIST OF REFERENCES

- [1] P. Paige, "SECNAV outlines five 'ambitious' energy goals," United States Navy, October 16, 2009. [Online]. Available: https://www.navy.mil/submit/display.asp?story_id=49044
- [2] United States Department of the Navy, "Department of the Navy's energy program for security and independence," October 2010. [Online]. Available: https://www.secnav.navy.mil/eie/ASN%20EIE%20Policy/Naval_Energy_Strategic_Roadmap.pdf
- [3] T. Takaishi, A. Numata, R. Nakano, and K. Sakaguchi, "Approach to high efficiency diesel and gas engines," *Mitsubishi Heavy Industries, Ltd. Technical Review*, vol. 45, no. 1, pp. 21-24, Mar. 2008. [Online]. Available: <https://pdfs.semanticscholar.org/3b35/8426f86e2ae7c667878f7c3c1de1b6747e12.pdf>
- [4] W. R. Fahrner and S. Schewertheim, "Semiconductor Thermoelectric Generators," *Materials Science Foundations*, vol. 61, 1-130, Aug. 2009, doi: 10.4028/www.scientific.net/MSFo.61.1.
- [5] S. O. Kasap, *Principles of Electronic Materials and Devices*, 4th ed. New York, NY, USA: McGraw-Hill, 2018, pp. 492-495.
- [6] S. Wiegand, "Introduction to thermal gradient related effects," in *Functional Soft Matter*, 2015. [Online]. Available: https://www.researchgate.net/publication/283322686_Introduction_to_thermal_gradient_related_effects_in_Functional_Soft_Matter
- [7] R. J. Moreno, A. G. Pollman, and D. Grbovic, "Harvesting waste thermal energy from military systems," in *Proceedings of the ASME Power and Energy Conference 2018 2* (Power2018-7514), Lake Buena Vista, FL, USA, 2018, pp. 1-6.
- [8] TEGpro, *TE-MOD-22W7V-56 22 Watt Thermoelectric Module*, 2014. [Online]. Available: <https://www.tegmart.com/datasheets/TGPR-22W7V-56S.pdf>
- [9] J. C. Bass, N. B. Elsner, and F. A. Leavitt, "Performance of 1 kW thermoelectric generator for diesel engines," *AIP Conference Proceedings*, vol. 316, no. 1, pp. 295-298, Aug. 1994. [Online]. Available: <https://aip-scitation-org.libproxy.nps.edu/doi/abs/10.1063/1.46818>

- [10] N. Baatar and S. Kim, "A thermoelectric generator replacing radiator for internal combustion engine vehicles," *Telkomnika*, vol. 9, no. 3, pp. 523-530, Dec. 2011. [Online]. Available: https://search-proquest-com.libproxy.nps.edu/docview/1010334737?rfr_id=info%3Axri%2Fsid%3Aprimo
- [11] D. Sivaprahasam, S. Harish, R. Gopalan, and G. Sundararajan, "Automotive waste heat recovery by thermoelectric generator technology," in *Bringing Theroelectricity into Reality*, P. Aranguren, London, UK: IntechOpen Limited, 2018, pp. 163-183. [Online]. Available: <https://www.intechopen.com/books/bringing-thermoelectricity-into-reality/automotive-waste-heat-recovery-by-thermoelectric-generator-technology>
- [12] C. D. Stokes, P. M. Thomas, N. G. Baldasaro, M. J. Mantini, R. Venkatasubramanian, M. D. Barton, C. V. Cardine, and G. W. Walker, "Thermoelectric Waste Heat Recovery from an M1 Abrams Tank," *SPIE Proceedings*, vol. 8377, May 2012, doi: 10.1117/12.920804.
- [13] N. Baranwal and S. P. Mahulikar, "Review of infrared signature suppression systems using optical blocking method," *Defense Technology*, vol. 15, pp. 432-439, Dec. 18, 2019. [Online]. doi: 10.1016/j.dt.2018.12.002
- [14] J. Thompson, D. Vaitekunas, and A. M. Birk, "IR signature suppression of modern naval ships," in *ANSE 21st Century Combatant Technology Symposium*, 1998. [Online]. Available: https://www.davis-eng.com/docs/papers/irss_paper.pdf
- [15] L. Howard, D. Grbovic, and A. Pollman, "Modeling and simulation approach to inform waste heat harvesting prototype for fossil fuel exhaust," in *Proceedings of 3rd International Conference on Energy Harvesting, Storage, and Transfer 2019*, Ottawa, Canada, 2019. [Online] doi: 10.11159/ehst19.134
- [16] Alexnld, "Universal black iron 2-3 kW exhaust muffler silencer for 5.5 HP 6.5 HP 3500 W 4000W gasoline generator." Apr. 16, 2020. [Online]. Available: https://alexnld.com/product/universal-black-iron-2-3kw-exhaust-muffler-silencer-for-5-5hp-6-5hp-3500w-4000w-gasoline-generator/?gclid=CjwKCAjwhOD0BRAQEiwAK7JHmO5wFQoSgnwLN8HEjVUZtvUaT7cy8dPkTsOuWgyjZRG4Rq9nMz3dIBoCYO0QAvD_BwE
- [17] DuroMax Next Generation Power Systems, "DuroStar DS4000S 4000-Watt 7-Hp air cooled OHV gas engine portable RV generator." Feb. 25, 2020. [Online]. Available: <https://www.duromaxpower.com/products/durostar-ds4000s-4000-watt-7-hp-air-cooled-ohv-gas-engine-portable-rv-generator>
- [18] Y.A. Cengel and M.A. Boles, *Thermodynamics: An Engineering Approach*, 5th ed. New York, NY, USA: McGraw-Hill, 2006, pp. 494-495.

- [19] F.P. Incropera, D.P. Dewitt, T.L. Bergman, and A.S. Lavine, *Fundamentals of Heat and Mass Transfer*, 6th ed. Hoboken, NJ, USA: Wiley, 2007, pp. 8, 9-10, 138-139, 147-150, 376, 405-410, 564, 571, 744-748, 762-763, 933-934, 941.
- [20] L. Howard, D. Tafone, D. Grbovic, and A. Pollman, “COMSOL Multiphysics simulation of TEGs for waste thermal energy harvesting,” in *COMSOL Conference 2018*, 2019. [Online] Available: <https://www.comsol.com/conference2018/download-paper/66172.pdf>
- [21] TEGMart, “Scientific guide to understanding thermoelectric generators and TEG products for converting heat to TEG power!” Apr. 20, 2020. [Online]. Available: <https://www.tegmart.com/info/guide-to-understanding-and-using-teg-power-and-products/>
- [22] MakeItFrom, “Dense zircon-based porcelain (IEC 60672 Type C-440)” Apr. 20, 2020. [Online]. Available: <https://www.makeitfrom.com/material-properties/Dense-Zircon-Based-Porcelain-IEC-60672-Type-C-440>
- [23] H. D. Young and R. A. Freedman, *Sears and Zemansky’s University Physics: with Modern Physics*, 11th ed. San Francisco, CA, USA: Addison & Wesley, 2004, pp. 951, 962, 986-989.
- [24] FLIR, *FLIR T1030sc*, 2015. [Online]. Available: <https://www.flir.com/globalassets/imported-assets/document/t1030sc-brochure-web-version.pdf>
- [25] L. B. Stotts, *Free Space Optical Systems Engineering: Design and Analysis*. Hoboken, NJ, USA: Wiley, 2017, pp. 128, 131.
- [26] H. Budzier and G. Gerlach, *Thermal Infrared Sensors: Theory, Optimisation and Practice*. West Sussex, UK: Wiley, 2011, pp. 45, 56, 117-119.
- [27] J. Huang, H. Kuo, and S. Shen, eds., *Nitride Semiconductor Light-Emitting Diodes (LEDs): Materials, Technologies, and Applications*, 2nd ed. (Woodhead Publishing Series in Electronic and Optical Materials). Duxford, UK: Elsevier, 2018, pp. 667.
- [28] Lynred by Sofradir and Ulis, *Scorpio LW*, 2019. [Online]. Available: <https://www.lynred.com/sites/default/files/2019-10/Scorpio-LW-datasheet.pdf>
- [29] Lynred by Sofradir and Ulis, *Daphnis-HD MW*, 2019. [Online]. Available: <https://www.lynred.com/sites/default/files/2019-10/Daphnis-HD-MW-datasheet.pdf>
- [30] D. E. Fletcher, G. Hobson, and J. Gordis, “Novel natural convection heat sink design concepts from first principles,” M.S. thesis, Dept. of Mech. Eng., NPS, Monterey, CA, USA, 2016. [Online]. Available: <http://hdl.handle.net/10945/49458>

THIS PAGE INTENTIONALLY LEFT BLANK

INITIAL DISTRIBUTION LIST

1. Defense Technical Information Center
Ft. Belvoir, Virginia
2. Dudley Knox Library
Naval Postgraduate School
Monterey, California